ACS PHYSICAL CHEMISTRY Au
AN OPEN ACCESS JOURNAL OF THE AMERICAN CHEMICAL SOCIETY

pubs.acs.org/physchemau

Article

Elucidation of Cu−Zn Surface Alloying on Cu(997) by Machine-Learning Molecular Dynamics

Harry H. Halim and Yoshitada Morikawa*

Cite This: *ACS Phys. Chem Au* 2022, 2, 430−447

Read Online

ACCESS | Metrics & More | Article Recommendations | Supporting Information

ABSTRACT: The Cu−Zn surface alloy has been extensively involved in the investigation of the true active site of $Cu/ZnO/Al_2O_3$, the industrial catalyst for methanol synthesis which remains under controversy. The challenge lies in capturing the interplay between the surface and reaction under operating conditions, which can be overcome given that the explicit dynamics of the system is known. To provide a better understanding of the dynamic of Cu−Zn surface at the atomic level, the structure and the formation process of the Cu−Zn surface alloy on Cu(997) were investigated by machine-learning molecular dynamics (MD). Gaussian process regression aided with on-the-fly learning was employed to build the force field used in the MD. The simulation reveals atomistic details of the alloying process, that is, the incorporation of deposited Zn adatoms to the Cu substrate. The surface alloying is found to start at upper and lower terraces near the step edge, which emphasize the role of steps and kinks in the alloying. The incorporation of Zn at the middle terrace was found at the later stage of the simulation. The rationalization of alloying behavior was performed based on statistics and barriers of various elementary events that occur during the simulation. It was observed that the alloying scheme at the upper terrace is dominated by the confinement of Zn step adatoms by other adatoms, highlighting the importance of step fluctuations in the alloying process. On the other hand, the alloying scheme at the lower terrace is dominated by direct exchange between the Zn step adatom and the Cu atom underneath. The alloying at the middle terrace is dominated by the wave deposition mechanism and deep confinement of Zn adatoms. The short propagation of alloyed Zn in the middle terrace was observed to proceed by means of indirect exchange instead of local exchange as proposed in the previous scanning tunneling microscopy (STM) observation. The comparison of migration rate and activation energies to the result of STM observation is also made. We have found that at a certain distance from the surface, the STM tip significantly affects the elementary events such as vacancy formation and direct exchange.

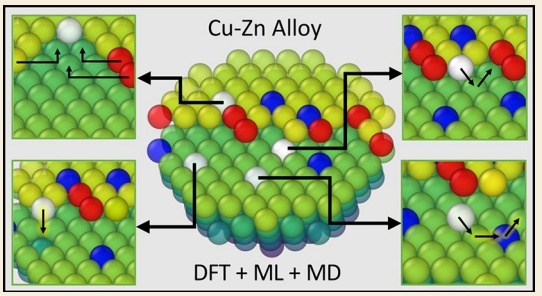

KEYWORDS: *Cu−Zn, surface alloy, density functional theory, molecular dynamics, machine learning, STM-tip effect*

1. INTRODUCTION

The catalysts based on metal alloys are well recognized in the world of heterogenous catalysis considering the emerging of unique properties upon alloying.[1,2] Given the optimal composition and environment, these catalysts can offer high catalytic performance, which outperform their alloy constituents. There have been notorious examples on the application of metal-alloy-based catalysts in heterogenous catalysis.[3−6] In the present study, we focus on the Cu−Zn surface alloy which has been reported to be very active for methanol synthesis by hydrogenation of CO_2.[7,8] Experimental studies have shown that the deposition of Zn on Cu(111) promotes the activity of methanol production by an order of magnitude at a Zn coverage of 0.19.[7,9] In addition, the Cu−Zn alloy has been reported as a good model of $Cu/ZnO/Al_2O_3$ (CZA),[8,17] the industrial catalyst used to synthesize methanol by hydrogenation of CO_2.[10] Thus, this alloy has been extensively involved in the investigation of the true active site of CZA which remains under controversy.[8,11−17]

In many previous computational studies, the Cu step surface decorated with Zn atoms was assumed as the surface model and became part of the rationalization of the experimental results.[8,11,13,18,19] The introduction of the surface defects (e.g., steps and kinks) in the computational model is based on previous computational and experimental studies which found that they play a critical role in improving the catalytic activity.[8,20,21] Meanwhile, the addition of Zn to the Cu steps also gives improvement in the catalytic activity as suggested by calculations;[4,8,11] however, the basis of assuming attached Zn at the rigid step edge has not been clearly justified due to the challenge in capturing the true surface property under reaction conditions. In fact, the STM experiments by Sano et al. indicated

Received: March 18, 2022
Revised: June 2, 2022
Accepted: June 2, 2022
Published: June 15, 2022

https://doi.org/10.1021/acsphyschemau.2c00017
ACS Phys. Chem Au 2022, 2, 430−447

that most of the Zn atoms are eventually substituted homogeneously into the terrace rather than localized at the step edge under vacuum conditions.[22] Further, it is well known that the Cu step adatom migrates intensively along the step edge, resulting in step fluctuation even at room temperature.[23,24] The assumption of a perfect step edge will also become invalid if the presence of adsorbates induces the reconstruction of the surface, the phenomenon that has been evidenced by various studies.[25−30] Therefore, the understanding of the realistic catalyst's surface is essential to provide a good assumption of the surface model and better interpretation of experimental data.

Another motivation of the present study is to rationalize the formation of the Cu−Zn alloy. Experimentally, it was clearly shown that the alloying is initiated at the upper terrace near the step edge before taking place at the middle terrace.[22] The mechanism to allow Zn propagation from the upper to middle terrace was proposed to be the local exchange between Zn and neighboring Cu atoms. However, the confirmation of such a proposal (i.e., the occurrence of local exchange) has remained elusive due to the challenge in capturing the fast and rare atomic events during the alloying. In fact, based on density functional theory (DFT) calculations, we found that such local exchange should be impractical even with the condition of high temperature as it is required to overcome a barrier of more than 2 eV (see Section 3.3.4). Therefore, we are motivated to revise the existing proposal and improve the current knowledge of the alloying process.

The atomic-level observation of the surface alloying in principle can be achieved through dynamic simulation of the surface under relevant working conditions. Given the active development of machine learning in material science,[31] it is now possible to construct a machine-learned force field with first-principles accuracy in exchange of computationally demanding ab initio molecular dynamics (AIMD). Some of the works have been successfully applied in the dynamic simulation of Cu-based catalysts.[32−35] In this framework, it is highly desirable to obtain the accurate force field with a minimum number of costly first-principles calculations. Thus, strategies called active learning and on-the-fly learning have been progressing in recent years.[36] The active-learning (or self-learning) framework allows the model itself to automatically select the datapoint to be included in the database, while the on-the-fly learning allows the iterative improvement of the model during simulation. These strategies are often coupled to obtain an accurate force field based on a compact database containing only the most representative structures. For instance, stochastic surface walking (SSW) global optimization, which can efficiently locate the structures in the transition state (TS) region, is used to generate important datapoints to be appended in the database, thereby allowing to improve the neural network (NN) potential iteratively during training.[37−39] This framework has successfully treated the complex potential energy surface (PES) involving high energy barriers such as catalytic reactions and phase transitions. Another implementation is achieved by means of the Query by Committee framework, in which multiple NN models are combined to seek for the disagreement that is used to give the error estimate of the prediction.[40] The structures that have the highest disagreement are then treated as important datapoints to be included in the database. Alternatively, the reliable uncertainty estimation can be directly calculated within the Gaussian process (GP) framework in the form of standard deviation (σ). This uncertainty is an intrinsic part of the framework and can be readily used with on-the-fly and active learning schemes. The GP-based framework has been successfully applied to build an efficient force field for investigating melting points,[41] phase transition of hybrid perovskites,[42] and atomistic rare events.[43]

Recently, it was reported that by coupling MD, active learning, and automated event detection, Lim et al. have successfully revealed the restructuring mechanisms of Pd deposited on Ag.[44,45] By adopting similar methodologies, we performed MD simulation of Zn depositions on the Cu(997) surface to explicitly capture the mechanisms that are responsible to the Cu−Zn surface alloying. The MD simulations were implemented based on a force field that was trained by means of GP. The database, containing information of atomic forces acting on various environments, was obtained from DFT calculations. The task of training was done by using the Fast Learning of Atomistic Rare Events (FLARE) code which utilizes the uncertainty information from GP, together with the active on-the-fly learning scheme to build the force field efficiently.[43]

The rest of this paper is organized in the following manner: in Section 2, we provide the computational details on the DFT, GP, and MD methods that we used. In Section 3, we present and discuss the results on the database used to build the GP force field, the structures and the time evolution of the alloy as obtained by MD, and the mechanistic analysis of surface reconstruction. Finally, in Section 4, we summarize and conclude our findings.

2. COMPUTATIONAL DETAILS

We used DFT calculations to provide forces of the central atom on each atomic environment. All DFT calculations were performed using the STATE code.[46,47] The electron−ion interaction was described by ultrasoft pseudopotentials.[48] The convergence threshold for energy is set to 10^{-9} Ha/atom. We took into account the van der Waals (vdW) interactions by applying the optB86b-vdW exchange−correlation functional[49] as implemented in the STATE code.[50] The lattice constant and surface energy of Cu(111) are calculated to be 3.6102 Å and 1.88 J/m^2, respectively. These values are in good agreement with experimental values of Cu lattice constant (i.e., 3.6149 Å)[51] and surface energy of Cu(111) (i.e., 1.83 J/m^2),[52] thus confirming the reliability of the chosen functional. Details on surface energy calculation can be found in Section S1 of the Supporting Information.

To construct the GP force field, we used the FLARE code with two- and three-body multispecies kernels.[43] The interaction cutoffs for two- and three-body kernels are set to 7.0 and 4.5 Å, respectively. The hyperparameters embedded to these kernels, namely, two-body signal variances ($\sigma_{s,2}$), two-body length scale (l_2), three-body signal variances ($\sigma_{s,3}$), three-body length scale (l_3), and noise hyperparameter (σ_n), were optimized by maximizing the log marginal likelihood using the BFGS algorithm as implemented in SciPy[53] used inside the FLARE code. The database is constructed by employing active and on-the-fly learning schemes that update the database based on uncertainty information calculated by GP. In order to provide new atomic environments to be candidates for the database, an MD code internal to FLARE is used to evolve atomic structures with 1 fs time step within the canonical (*NVT*) ensemble. The temperature is set up at 700 K with all atoms allowed to move. To obtain more diverse atomic environments, we manually changed the initial structure after certain MD steps during the on-the-fly learning when no significant improvement in the mean absolute error (MAE) was found. The details of this

https://doi.org/10.1021/acsphyschemau.2c00017
ACS Phys. Chem Au 2022, 2, 430−447

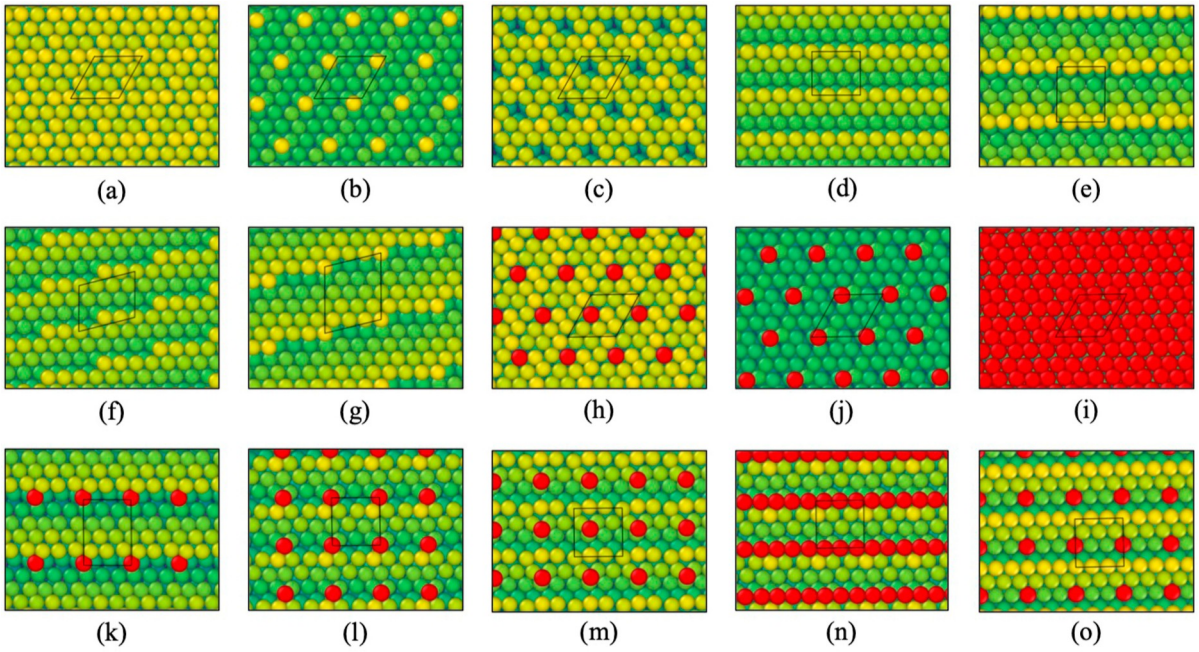

Figure 1. Parent structures used in the simulation: (a) Cu(111), (b) Cu(111) with Cu adatoms, (c) Cu(111) with vacancies, (d) Cu(221), (e) Cu(211), (f) Cu(111) with a kinked step edge of the (100) microfacet, (g) Cu(111) with a kinked step edge of the (111) microfacet, (h) Cu(111) with substituted Zn atoms, (i) Cu(111) with Zn adatoms, (j) Cu(111) with a Zn overlayer, (k) Cu(211) with Zn adatoms attached to the step edge, (l) Cu(221) with Zn adatoms attached to the step edge, (m) Cu(221) with diffusing Zn adatoms at the upper terrace, (n) Cu(221) with Zn step adatoms, and (o) Cu(221) with Zn adatoms incorporated near the step edge. The green to yellow color indicates Cu atoms, while the red color indicates Zn atoms. The black box shown in each figure depicts the unit cell of the structure.

procedure and the resulting database are reported in the next section. When the GP database is completed, the two- and three-body mean predictions are mapped onto cubic spline models using the mapped gaussian process (MGP) method[54] with uniform 64 control points and a 20 × 20 × 20 grid of control points for the two-body mean function and the three-body mean function, respectively. The resulting MGP potential is then used as a pair style in a large-scale MD simulation code, Large-scale Atomic/Molecular Massively Parallel Simulator (LAMMPS),[55] by which we performed MD simulations within the *NVT* ensemble with a time step of 5 fs.

The analysis of MD simulations to extract the non-equilibrium information is built using a combination of a homemade Python code,[56] Ovito,[57] and Atomic Simulation Environment (ASE).[56] Clamping the atoms to the particular sites is necessary to ease the analysis process by removing the thermal noise.[44,45] Thus, in this study, we clamped all the atoms to the nearest fcc sites based on the structure of Cu. All the MD images shown in this work were already clamped to aid the understanding of the alloyed structure. The images depicting Cu and Zn atoms were generated using Ovito.

3. RESULTS AND DISCUSSION

3.1. Construction and Evaluation of the Training Database

We constructed the database using active and on-the-fly learning schemes as implemented in the FLARE code. Each datapoint in the database is a local atomic environment with the corresponding atomic forces. Specifically, an atomic environment constitutes all two-body and three-body clusters found within a certain cutoff radius from a central atom, which we specified to be 7 and 4.5 Å for two-body and three-body cutoffs, respectively. Within active and on-the-fly learning schemes, the new data containing the local atomic environment and the associated force are appended to the database whenever the uncertainty is higher than a specified threshold. The new atomic environments are continuously generated from the MD simulations based on the iteratively updating GP force field. In more detail, the procedure to construct the database is as follows:

(i) First, we constructed four layers of the Cu(111) surface (Figure 1a), which represents the most common environment in the Cu(997) surface. The atomic forces of this structure are then calculated by DFT, and some atomic environments are randomly selected to populate the empty database.

(ii) Next, the resulting database is used in the GP framework to construct the temporary force field used in MD simulation. The MD within the *NVT* ensemble is used to generate new trajectories at a temperature of 700 K based on Cu(111) as the initial structure. Such an initial structure is what we call the parent structure since it is used to generate additional structures as candidates for the database.

(iii) At each MD step, all the atomic environments found in the trajectory are examined. If the uncertainty of the environment is higher than the noise hyperparameter (σ_n), the DFT calculation is performed and such an environment with the corresponding atomic forces is appended to the database. Otherwise, the database is not updated and the MD step continues. All the hyperparameters embedded in the kernel (i.e., $\sigma_{s,2}$, l_2, $\sigma_{s,3}$, l_3, and σ_n) are re-optimized whenever the database is updated. This routine is implemented in the FLARE code. More details on the equations used to calculate force and uncertainty, updating hyperparameters, and the description of the datapoints included in the database can be

https://doi.org/10.1021/acsphyschemau.2c00017
ACS Phys. Chem Au 2022, 2, 430−447

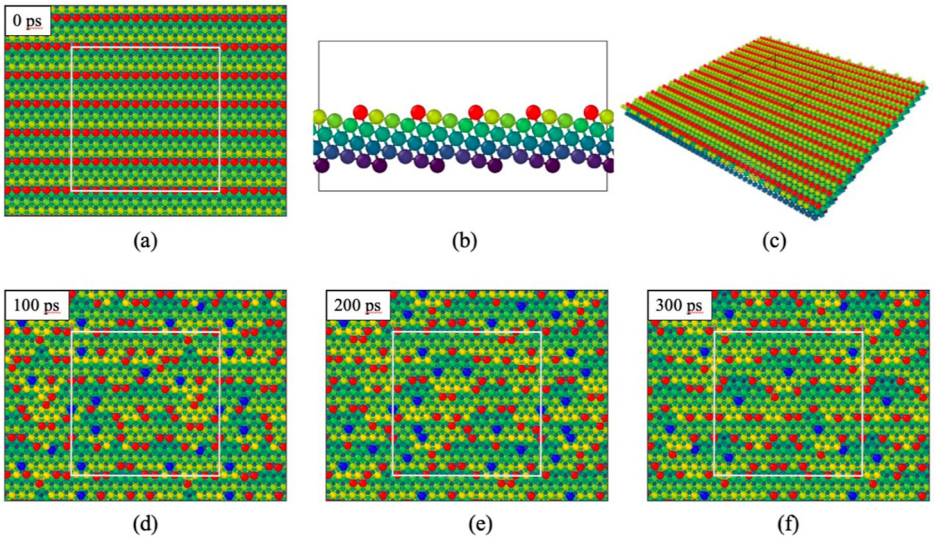

Figure 2. (a) Top view of Zn-deposited Cu(221), (b) side view of Zn-deposited Cu(221), (c) perspective view of Zn-deposited Cu(221), and (d–f) snapshots of MD simulation at 100, 200, and 300 ps of Zn-deposited Cu(221) within the *NVT* ensemble at 700 K. The green to yellow atom indicates the Cu atoms, the red atom indicates Zn as adatoms, and the blue atom indicates substituted Zn atoms. The box shown in each figure depicts the unit cell of the structure.

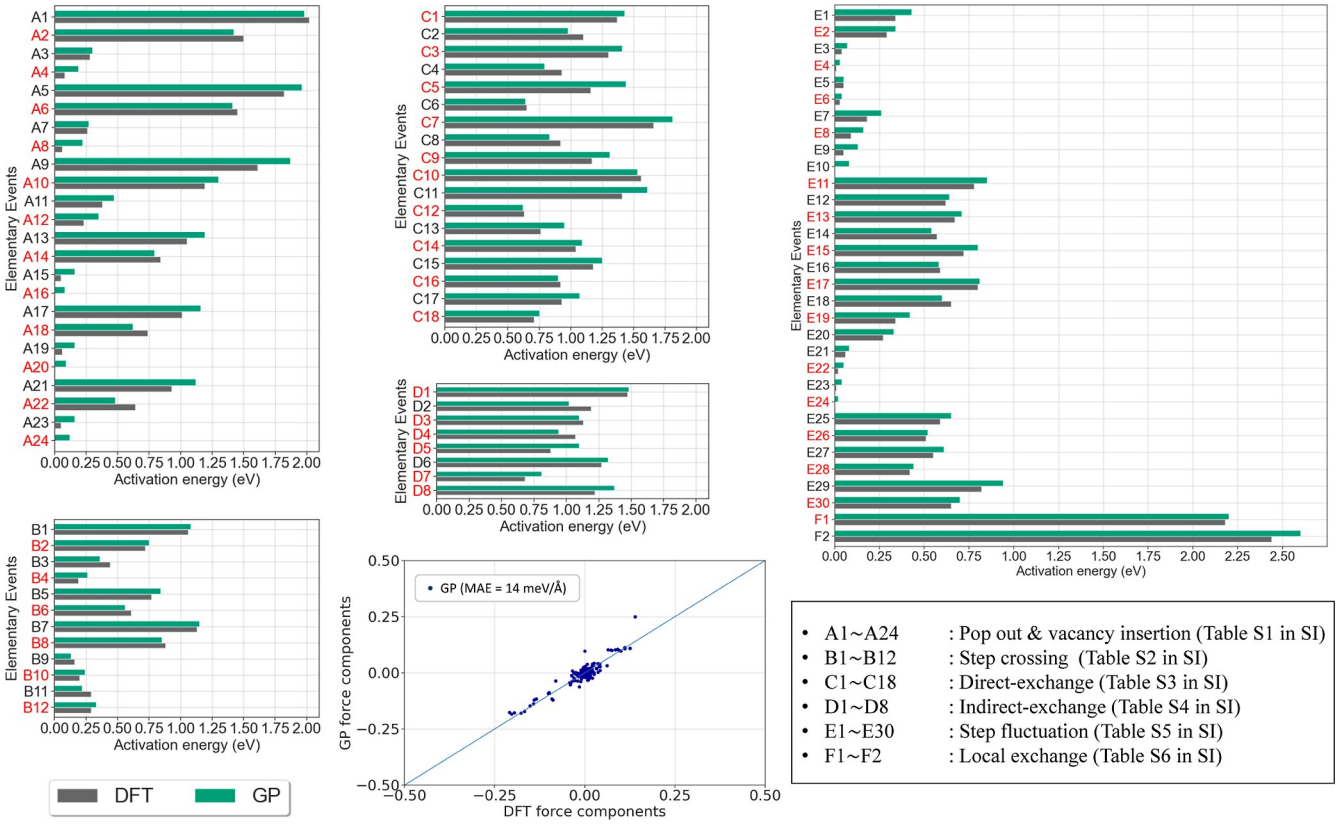

Figure 3. Activation energies obtained from DFT and GP for elementary events involving only Cu atoms (indicated by black indices) and mixed Cu-Zn atoms (indicated by red indices). The description of the indices is presented as a text box at the bottom right of the figure.The parity plot presented in the middle bottom shows the comparison between DFT and GP forces of the TS structures in each investigated elementary event.

found in ref 43 and also in Section S2 of the Supporting Information.

(iv) Since the MD simulation of Cu(111) is not sufficient to capture the vast variation of the environment in the target structure [i.e., Zn−Cu(997) surface], we gradually increase the complexity of the parent structure with features such as steps, kinks, and Zn atoms. All the structures consist of four layers with at least 30 Å vacuum region between two neighboring slabs in the *z*-direction. The top view and the corresponding unit cell of the parent structures are depicted in order in Figure 1. The training is performed sequentially through all these parent structures. For instance, after no high-uncertainty structure is found using the first parent structure [i.e., Cu(111)

https://doi.org/10.1021/acsphyschemau.2c00017
ACS Phys. Chem Au 2022, 2, 430−447

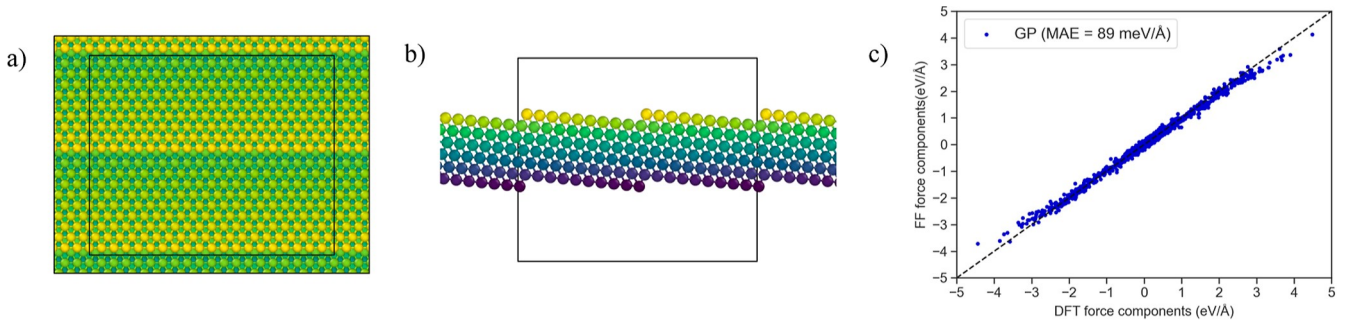

Figure 4. (a) Top view of Cu(997), (b) side view of Cu(997), and (c) parity plot showing the GP and DFT atomic forces of the center atoms in the environments with the highest uncertainties. The validation set consists of 1071 data points which correspond to the *x*, *y*, and *z* force components of each center atom in the 357 environments with the highest uncertainty found in 2 μs MD simulations of the more realistic Zn-deposited Cu(997) surface.

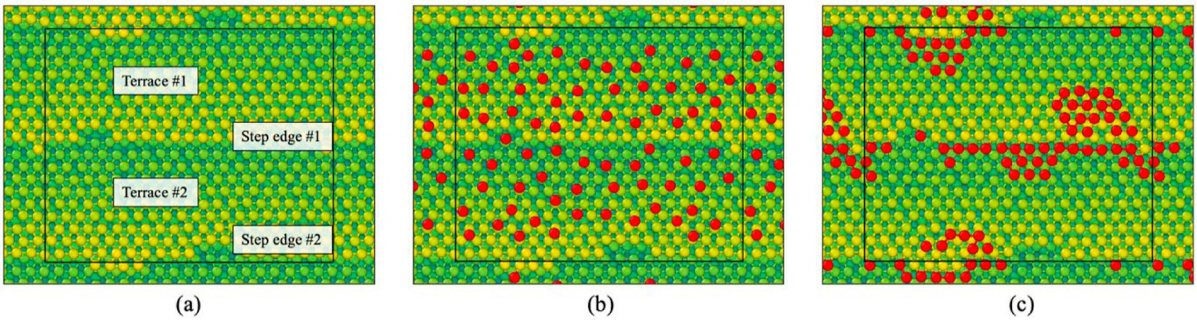

Figure 5. Preparation of the Zn-deposited Cu surface. The green to yellow atom indicates Cu atoms, while the red atom indicates Zn atoms. (a) Clean Cu(997) surface which features steps and kinks obtained after annealing. (b) Zn atoms are randomly deposited on the clean surface at 300 K. (c) Some of the Zn atoms attach to the step edge, while some others agglomerate into small islands at the upper terrace.

surface], the parent structure is replaced with the more complex one [i.e., Cu(111) surface with adatoms] and then stages (ii) and (iii) are repeated. In total, the training data consisting of 301 environments that have passed 15 parent structures in Figure 1 are obtained.

(v) To further search for the local environment that possibly appears during Zn alloying on Cu(997), we significantly enlarge the size of the parent structure to four layers of the Cu(221) surface with five step edges and 15 atoms in every row per unit cell, as shown in Figure 2a–c. This model is chosen since it has denser steps, thereby allowing more step-edge-related events to happen. We then deposited Zn on top of the surface and let the system evolve within the *NVT* ensemble at 700 K for 300 ps. The evolution of this structure is shown in Figure 2d–f. The environments of the moving atom in the resulting trajectories are sampled, and their uncertainties are calculated. We then manually added 25 more environments with the highest uncertainty to the database. Each of these new environments has 7 Å cutoff radius from the central atom. Due to the expensive cost of DFT calculations, we could not perform DFT calculations on this large system. Instead, we sliced the region near the central atom of the atomic environment to obtain smaller unit cells ($15.32 \times 15.32 \times 30$ Å^3) and performed the DFT calculation based on this small cell.

In the end of training, our final database consists of 326 atomic environments. The final optimized GP hyperparameters are 0.125 eV/Å for two-body signal variances ($\sigma_{s,2}$), 0.001 eV/Å for three-body signal variances ($\sigma_{s,3}$), 0.750 Å for two-body length scale (l_2), 1.068 Å for three-body length scale (l_3), and 0.037 eV/Å for the noise hyperparameter (σ_n).

To evaluate the accuracy of the force field, we compared the GP versus DFT barriers of various elementary events including pop out and vacancy insertion, step crossing, direct exchange, indirect exchange, events related to step fluctuations, and the local-exchange mechanism as defined in Table S1–S6 of the Supporting Information. The comparison between DFT and GP barriers is shown in Figure 3. The MAEs of barriers of elementary events involving Cu as the active atom (indicated by black indices in Figure 3) and elementary events involving Zn as the active atom (indicated by red indices in Figure 3) are calculated to be 70 and 88 meV, respectively. We noted that in the active and on-the-fly learning employed in this work, we do not explicitly search for the TS region. The main principle of the learning scheme employed in this work is to selectively include the structures with high uncertainty that is calculated within the GP framework (see eq S2 in the Supporting Information). In the case of more complicated PESs such as in phase transition and chemical reactions, methods such as SSW can be used to sample the PES efficiently at the TS region and thus help to improve the consistency of the barrier between DFT and the force field.[37−39] Aside from the barrier, we also calculated the MAE of the force in the TS structures and found the MAE to be 14 meV/Å, as shown by the parity plot at the middle bottom of Figure 3.

In addition, we calculated the force component's MAE of 357 environments with the highest uncertainty found in 2 μs MD simulations of the more realistic Zn-deposited Cu(997) surface. The Cu(997) structure has 6 layers and consists of 2352 atoms with 2 step edges and 20 atoms in every row per unit cell. The top and side views of such surface are shown in Figure 4a,b,

https://doi.org/10.1021/acsphyschemau.2c00017
ACS Phys. Chem Au 2022, 2, 430−447

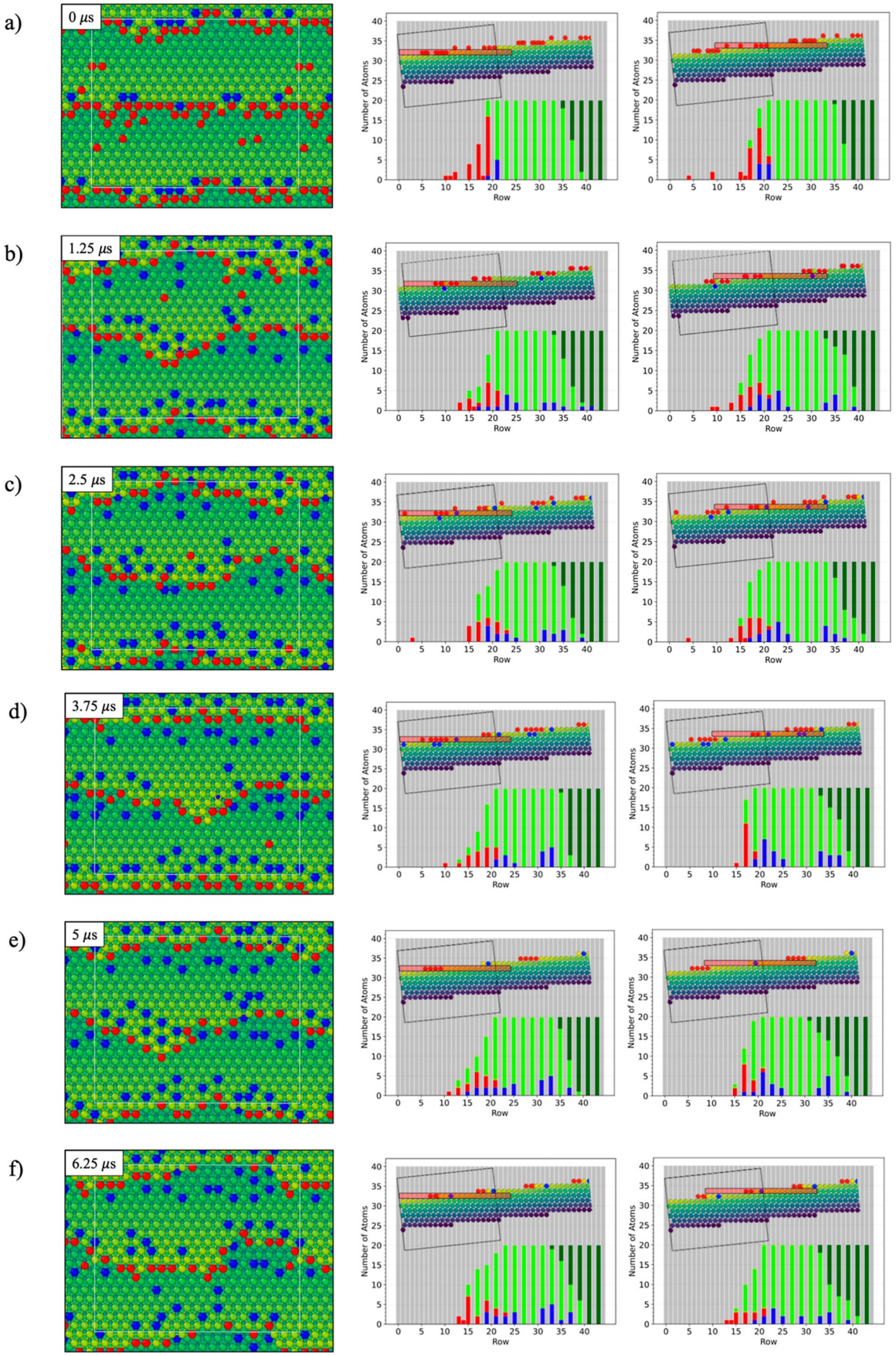

Figure 6. Snapshots of MD simulations showing the evolution of deposited Zn atoms on Cu(997) at 700 K. The green to yellow atoms indicates the Cu atoms, the red atoms indicates Zn as adatoms, and the blue atoms indicates substituted Zn atoms. The two plots accompanying each snapshot show the

https://doi.org/10.1021/acsphyschemau.2c00017
ACS Phys. Chem Au 2022, 2, 430−447

Figure 6. continued

composition of atoms as a function of rows. In each plot, the red, blue, light-green, and dark-green bars indicate the number of Zn as adatoms, Zn as incorporated atoms, Cu as surface atoms, and the Cu atom which is covered by an additional Cu or Zn layer (i.e., Cu sub-surface). (a) Zn adatoms are found to localize at the step edge shortly after the deposition. (b–e) At 1.25 to 5 μs, the Zn atoms incorporate the surface at the region near the step edge. (f) At 6.25 μs, the Zn incorporated atoms are found at the middle terrace.

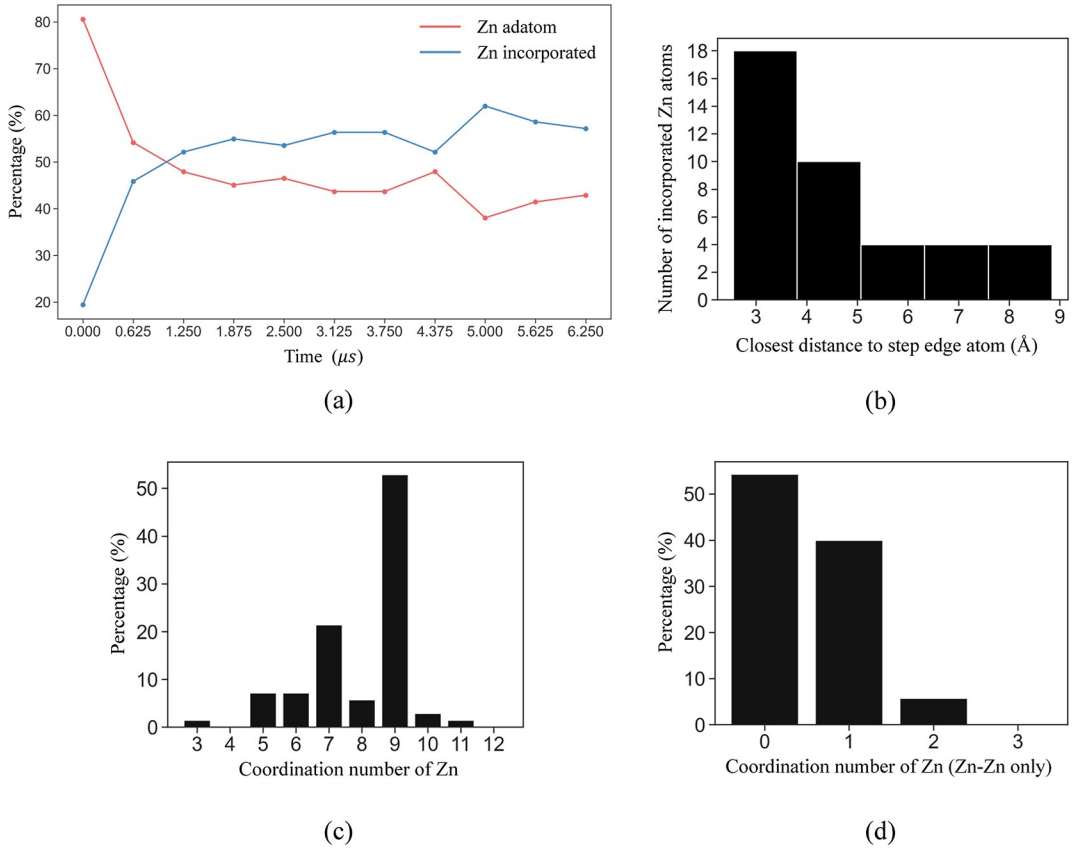

Figure 7. Analysis of the structure of the Cu–Zn surface. (a) Change in percentage of Zn adatoms versus Zn incorporated over time. (b) Histogram of the relative distance between incorporated Zn atoms and the step edge. (c) Distribution of the Zn coordination number, accounting the Zn bonding with other Cu and Zn neighboring atoms. (d) Coordination number of Zn atoms but accounting only the Zn–Zn coordinations.

respectively. The three bottommost layers are fixed with the lattice constant obtained from DFT calculations (i.e., 3.6102 Å), which is in good agreement with the experimental lattice constant of Cu (i.e., 3.6149 Å).[51] To provide the DFT forces, we again sliced the original unit cell of Cu(997) near each central atom to obtain smaller cells containing the environments with the highest uncertainty. These smaller cells then are used in the DFT calculations with periodic boundary conditions. We obtained the resulting MAE to be 89 meV/Å. The parity plots are presented in Figure 4c.

3.2. Evolution of Deposited Zn Atoms on Cu(997)

3.2.1. Preparation of the Surface. In order to observe the formation process of the Cu–Zn surface alloy, we performed MD simulations of the Cu(997) surface with 0.19 coverage of deposited Zn atoms. Such Zn coverage has been observed in experiments to give an optimum turn over frequency for methanol synthesis.[7,9] There are two terraces and two step edges for each unit cell as indicated in Figure 5a. The Zn atoms are then deposited randomly on top of the surface at 300 K (Figure 5b). After the equilibration for several nanoseconds, we found that the randomly distributed Zn atoms either attach to the step edges or form Zn islands on the upper terrace (Figure 5c). Such a structure is in good agreement with the scanning tunneling microscopy (STM) observation that suggested the localization of Zn atoms around the step and the formation of small Zn islands on the terraces after Zn deposition.[22] After that, we increased the temperature to 550 K and again equilibrated the surface for 20 ns. The island of Zn atoms then collapses, and a majority of the Zn atoms now attach to the step edge though some others still can be found at the terrace in the form of diffusing atoms (Figure 6a). This surface structure was then used to observe the Cu–Zn surface alloying process at 700 K.

3.2.2. Surface Profile (MD Frames). To observe the alloying process of Cu–Zn, we performed MD simulations within the *NVT* ensemble at a temperature of 700 K for up to 6.25 μs. Figure 6a–f shows the evolution of deposited Zn atoms on Cu(997) until the Cu–Zn surface alloy is formed. To clearly observe the number of Zn atoms substituted at the terrace, we also plotted the composition of Cu and Zn atoms as a function of rows for every certain time step. Such plots accompany each MD snapshot in Figure 6a–f. The snapshots of the MD simulation are also presented as videos in the Supporting Information.

In the beginning (Figure 6a), the Zn atoms are found to localize at the step edge, covering the original Cu step adatoms. The profile of the boundary between Cu and Zn is still fairly

https://doi.org/10.1021/acsphyschemau.2c00017
ACS Phys. Chem Au 2022, 2, 430–447

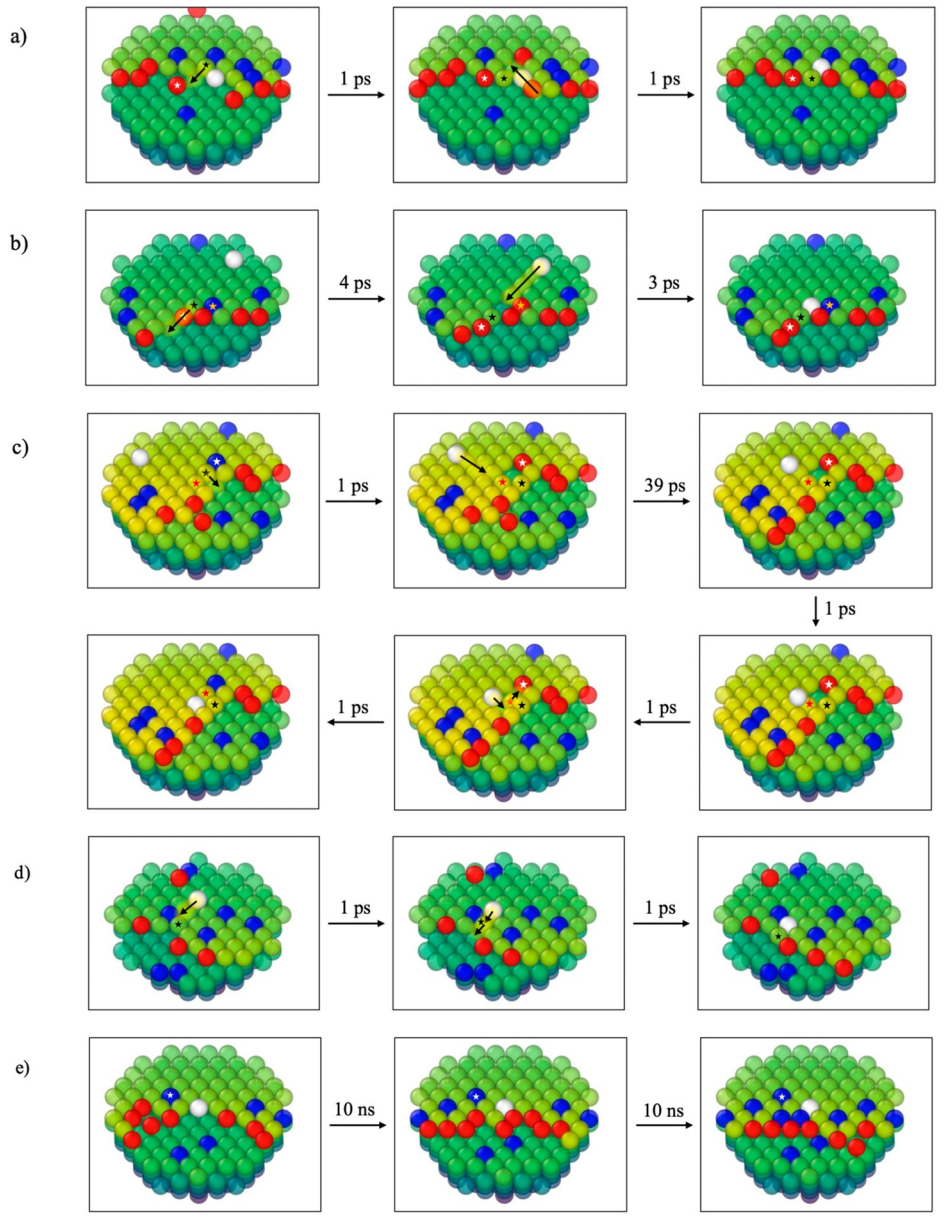

Figure 8. Alloying scheme at the upper terrace. The green to yellow atoms indicate Cu atoms, the red atoms indicates Zn as adatoms, and the blue atoms indicates substituted Zn atoms. The white atom indicate the moving Zn atom. Several atoms are marked with star-shaped symbol to ease the tracking of their positions. (a) Temporary vacancy formed by detaching Cu step adatoms is then occupied by nearby Zn step adatoms. (b) Zn atom fills the vacancy at the upper terrace by hopping descend. (c) Zn atom fills the vacancy at the upper terrace by exchange descend. (d) Zn atom descending the step edge by kicking another step adatom. (e) Zn step adatom is confined by other step adatoms.

linear. After 1.25 μs, some of the Zn atoms are incorporated at the upper and lower terraces near the step edge (Figure 6b). At this stage, almost no Zn atoms are incorporated at the middle terrace. We also noticed that Zn atoms are dominantly incorporated to the upper terrace, whereas only few incorporated Zn atoms are found at the lower terrace. After 2.5 μs (Figure 6c), the distribution of Zn on the surface and the number of incorporated Zn atoms are still relatively similar.

The change in the percentage of Zn adatoms versus Zn incorporated over time is shown in Figure 7a. Shortly after the deposition, almost all Zn atoms are in the state of adatoms as indicated by the contrast percentage between Zn adatoms and incorporated Zn at the early time. The Zn atoms then incorporate the Cu surface over time, decreasing the percentage of Zn adatoms until nearly half of the original number. The change in percentage is shown to be saturated around 2 μs, but the fluctuation is clearly observed in the following time. This indicates that the interchanges between Zn adatoms and incorporated Zn still actively occur during the simulation.

We found shallow incorporation of Zn to the subsurface layer, for instance, at time 1.25 μs (Figure 6b) and at time 3.75 μs (Figure 6d). However, the subsurface incorporated Zn cannot penetrate further to the bulk, and eventually, they transform back into adatoms or surface atoms as indicated by succeeding snapshots. This is consistent with the experimental finding in which no dissolution of Zn to the bulk was observed.[22] At 6.25 μs, finally, we found that some of the Zn atoms are incorporated at the middle terrace (Figure 6f). The trend observed in this simulation thus suggests that alloying is initiated at the upper and lower terraces near the step edge before taking place at the

https://doi.org/10.1021/acsphyschemau.2c00017
ACS Phys. Chem Au 2022, 2, 430−447

middle terrace at a later time. At the end of simulation, 2 out of 72 Zn atoms (2.78%) are desorbed from the surface.

To see the distribution of incorporated Zn atoms more clearly, we show in Figure 7b the distance of the incorporated Zn atoms relative to the step edge at 6.25 μs. As shown in the figure, most of the Zn incorporates the surface at the region near the step edge, which indicates that the alloying dominantly occurs near the step edge and thus, the step edge plays an important role in the alloying. Sano et al. observed that the alloying of Cu−Zn at or above 523 K leads to the homogeneous distribution of Zn into the Cu(111) surface layer.[22] However, since our MD simulation requires a short time step, it is infeasible to simulate the alloying at the timescale longer than what we have performed (i.e., 6.25 μs). Thus, we are not able to reproduce the homogeneous distribution of Zn into the Cu surface. The simulation with a longer time scale can be achieved, for instance, with kinetic Monte Carlo (KMC) simulation.[58] Nevertheless, we managed to observed the incorporation of Zn atoms and elucidate the corresponding mechanisms. We also list DFT barriers of various elementary events (see Section S3 of the Supporting Information) that contribute to the alloying, which can be used as parameters in the KMC. More detailed discussion on the mechanistic aspect of the alloying and the role of step edge are presented in the next section.

The distribution of the Zn coordination number at 6.25 μs, accounting all the Zn bonding with other Cu and Zn neighboring atoms, is shown in Figure 7c. Almost all the incorporated Zn atoms have 9 coordination number, which indicates that they stay at the surface. Few of the Zn atoms have coordination numbers of 10 and 11, which means that they are almost buried by the surface atoms. On the other hand, the coordination number of Zn adatoms varies from 3 to 8 as they are distributed along the wavy step edge. Figure 7d shows the coordination number of Zn atoms at 6.25 μs but accounting only the Zn−Zn coordinations. The histogram depicted in the figure shows that Zn is mostly surrounded by the Cu atoms and thus, there is no significant Zn−Zn interaction in the resulting alloy, consistent with the analysis from STM observation.[22]

3.3. Alloying Mechanisms (Energetics, Classification, and Statistics)

In this section, we discuss in detail the alloying schemes of Zn that were observed during MD simulation. These schemes describe how Zn in the form of adatoms turns into incorporated atoms and is thus "alloyed" into the surface. We categorize the schemes based on three regions where the incorporation occurs: upper terrace, lower terrace, and middle terrace. We also show examples of each in-operation scheme that were observed during simulation. All the observed alloying events are reported as short videos in the Supporting Information.

3.3.1. Alloying at the Upper Terrace. Alloying at the upper terrace is dominant in the early stage of alloying, which is mainly caused by two factors: the localization of Zn at the step edge after the deposition and the fluctuation of the step adatoms. The observation of Zn alloying at the upper terrace as the initial alloying stage was also reported by Sano et al. by means of STM observations.[22] Based on our simulation, we found three schemes responsible to the alloying at this region: (i) vacancy insertion at the upper terrace, (ii) exchange descend, and (iii) confinement by other step adatoms. The characteristics of these schemes are described as follows.

3.3.1.1. Vacancy Insertion at the Upper Terrace. Vacancies at the upper terrace might be formed by means of detachment of step adatoms or the pop out of surface atoms. Such vacancy may occasionally preserve for a certain time period and attract the nearby Zn adatom. By using a simplified model, we calculated the barrier of the vacancy formation by detachment of Cu and Zn adatoms from the step edge to be 0.80 eV (event no. E17 in Table S5) and 0.65 eV (event no. E18 in Table S5), respectively. Meanwhile, the barriers to form the vacancy through the atom pop out at the upper terrace are higher as we found more than 1 eV barrier for both Cu and Zn pop out (event no. A5 and A6 in Table S1).

We observed that there are several ways for Zn atoms to occupy the vacancy: lateral exchange, vacancy hopping descend/simple-vacancy insertion, and vacancy exchange descend. In lateral exchange, the step adatom diffuses away toward the lower terrace and subsequently leaves a vacancy which is then occupied by the nearby Zn step adatom (Figure 8a). In contrast with lateral exchange, the vacancy hopping descend (Figure 8b) and vacancy exchange descend (Figure 8c) require the diffusing Zn adatom on the upper terrace. The source of this terrace adatom can be varied, for instance, Zn hopping ascend (event no. B2 in Table S2), Zn exchange ascend (event no. 6 in Table S2), and detachment of Zn step adatoms from a higher step edge (event no. E14 in Table S5). Such mechanisms have barriers of 0.72, 0.61, and 0.57 eV, respectively. The Zn terrace adatom is very unlikely to be formed by atomic pop out from the upper terrace (event no. A6 in Table S1) or middle terrace (event no. A2 in Table S1) considering more than 1 eV barrier for both cases. The barrier of the vacancy insertion by Zn is typically small; thus, the energy cost of this scheme mainly comes from the formation of vacancy at the upper terrace or diffusing terrace adatoms.

3.3.1.2. Exchange Descend. In this scheme, the Zn terrace adatom near the descending step edge pushes the step adatom underneath toward the lower terrace and then takes its position (Figure 8d). The Zn exchange descend has a modest barrier of 0.20 eV (event no. B10 in Table S2) in the presence of a straight edge and slightly higher in the presence of a kinked edge as we found barrier of 0.30 eV (event no. B12 in Table S2). Despite the modest barrier, the exchange descend also requires the Zn adatom to be on the upper terrace, similar to vacancy hopping descend and vacancy exchange descend.

3.3.1.3. Confinement by Other Step Adatoms. Another alloying scheme at the upper terrace is the confinement of Zn step adatoms by the other Cu or Zn step adatoms (Figure 8e). It is well known that the Cu step adatom migrates intensively along the step edge, resulting in step fluctuation even at room temperature.[23,24] In addition, the previous STM observation also reported the increase of density and waviness of the step after the deposition of Zn.[22] By calculating the barrier of elementary events of step edge fluctuations (i.e., attachment and detachment of adatoms to/from the step edge), we found that all the elementary events involving Zn atoms (all events in Table S5) have a lower barrier than the pure Cu system, suggesting that Zn atoms enhance the step edge fluctuations.

We identified 75 alloying events that take place at the upper terrace and counted the occurrence of the first and second schemes to be 12 and 44 events, respectively. Additionally, in all 75 alloying events, we found that the Zn atoms are eventually confined by more step adatoms for a certain period of time, considering the high intensity of step fluctuation. Thus, we considered the third scheme (i.e., confinement by other step adatoms) as the dominant scheme for the alloying at the upper terrace. The smaller percentage of the first and second schemes

https://doi.org/10.1021/acsphyschemau.2c00017
ACS Phys. Chem Au 2022, 2, 430−447

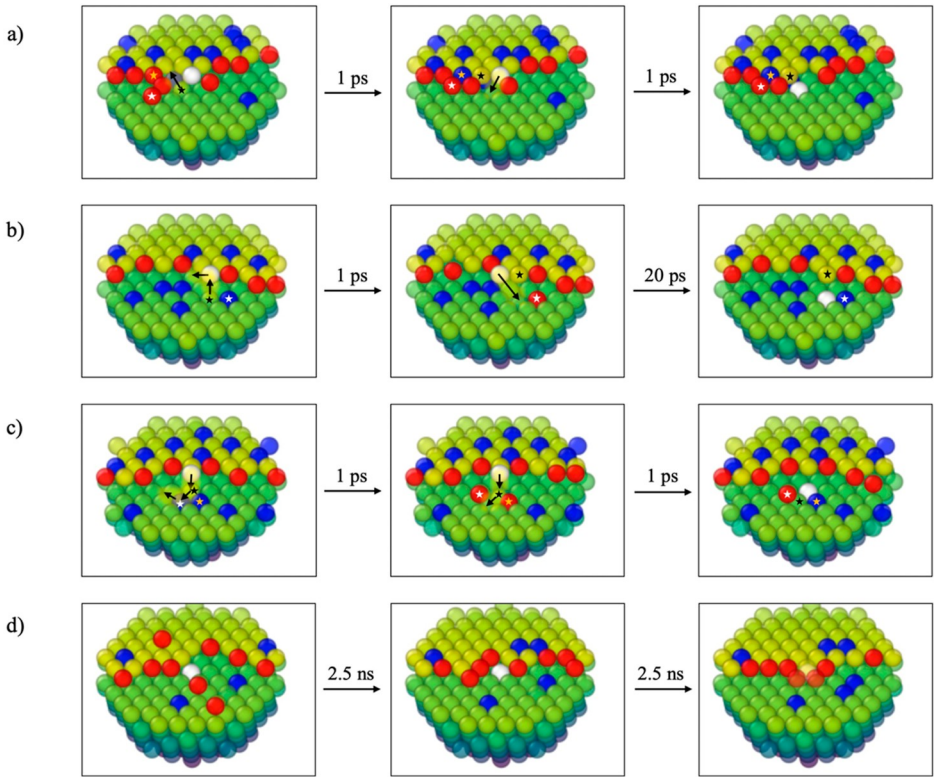

Figure 9. Alloying scheme at the lower terrace. The green to yellow atoms indicate Cu atoms, the red atoms indicates Zn as adatoms, and the blue atoms indicates substituted Zn atoms. The white atom indicate the moving Zn atom. Several atoms are marked with star-shaped symbol to ease the tracking of their positions. (a) Zn atom kicks out and takes the position of the Cu adatom underneath. (b) Zn step adatom fills the vacancy at the lower terrace. (c) Zn adatom influences the Cu adatom underneath to push the adjacent Zn-substituted atom. (d) Incorporated Zn atom at the lower terrace is buried by other step adatoms.

is attributed to the high barrier for the formation of vacancy and terrace adatoms on the upper terrace. Despite the high frequency, the third alloying scheme only results in the shallow Zn incorporation to the upper terrace; thus, the alloyed Zn can easily transform back into step adatoms when the confining atoms move away.

The alloying at the upper terrace which is induced by step fluctuation and vacancy diffusion was found in the case of Mn alloying on Cu(100), suggested by STM images and Monte Carlo simulation.[59,60] However, in contrast to Mn/Cu(100), alloying of Zn by the step fluctuation is not accompanied by the frequent alloying vacancy diffusions as evidenced by the low frequency of alloying by means of vacancy insertion at the upper terrace. We noticed that Zn can be incorporated simply through confinement by fluctuating adatoms as shown in Figure 8e.

3.3.2. Alloying at the Lower Terrace. The alloying of Zn at the lower terrace was found by means of STM observations by Bikaljevic et al. in the form of a roughened area, which was interpreted as the intermixing region between Cu and Zn.[61] Similarly, we also observed the formation of the alloy together with the associated alloying scheme at this region. We found three dominant alloying schemes for this case: (i) step-assisted direct exchange, (ii) vacancy insertion at the lower terrace, and (iii) indirect-exchange mechanism. The characteristics of this scheme are described as follows.

3.3.2.1. Step-Assisted Direct Exchange. In this scheme, the Zn step atom kicks out the surface atom at the lower terrace and takes its position (Figure 9a). The kicked atom then might diffuse away or attach to the step edge. By DFT calculations, we examined three types of step-assisted direct exchange. Type 1 is direct exchange which is initiated by the Zn step adatoms, resulting in the formation of Cu terrace adatoms. Type 2 is direct exchange which is initiated by Zn terrace adatoms, resulting in the formation of Cu step adatoms. Type 3 is direct exchange which is initiated by Zn step adatoms, resulting in Cu step adatoms. The barriers of direct-exchange type 1, type 2, and type 3 (event no. C11, C13, and C15 in Table S3) are 1.41, 0.76, and 1.14 eV, respectively. Even though type 2 has the lowest barrier, the requirement of Zn terrace adatoms suppresses its occurrence since an additional barrier to form Zn terrace adatoms is necessary. In fact, all the step-assisted direct-exchange schemes that we found are closer to type 3, in which the kicked Cu atom subsequently attaches to the step edge. We also observed the positive contribution of the kink site to this scheme as we found that the barrier reduces to 0.93 eV (event no. C17 in Table S3). In a previous study of the Pd−Ag alloy, the step-assisted direct-exchange scheme was found to predominantly occur in the early stage of restructuring, in connection with a small barrier of 0.29 eV, of which the final state is more stable by around 1 eV for the mechanism at the lower terrace near the kink site.[45] In contrast, in the case of Cu−Zn surface alloying, a similar mechanism near the kink site has a much higher barrier of 0.93 eV with the final state less stable by 0.22 eV. This trend is in agreement with the cohesive energy of Cu and Ag, in which Ag has a lower cohesive energy (2.95 eV/atom) compared to Cu (3.49 eV/atom).[62]

3.3.2.2. Vacancy Insertion at the Lower Terrace. This scheme is initiated by the vacancy generated by the pop out of surface atoms at the lower terrace. Once the vacancy is generated, the nearby Zn adatom at the step edge then fills the vacancy and hence alloyed into the surface (Figure 9b). In

https://doi.org/10.1021/acsphyschemau.2c00017
ACS Phys. Chem Au 2022, 2, 430−447

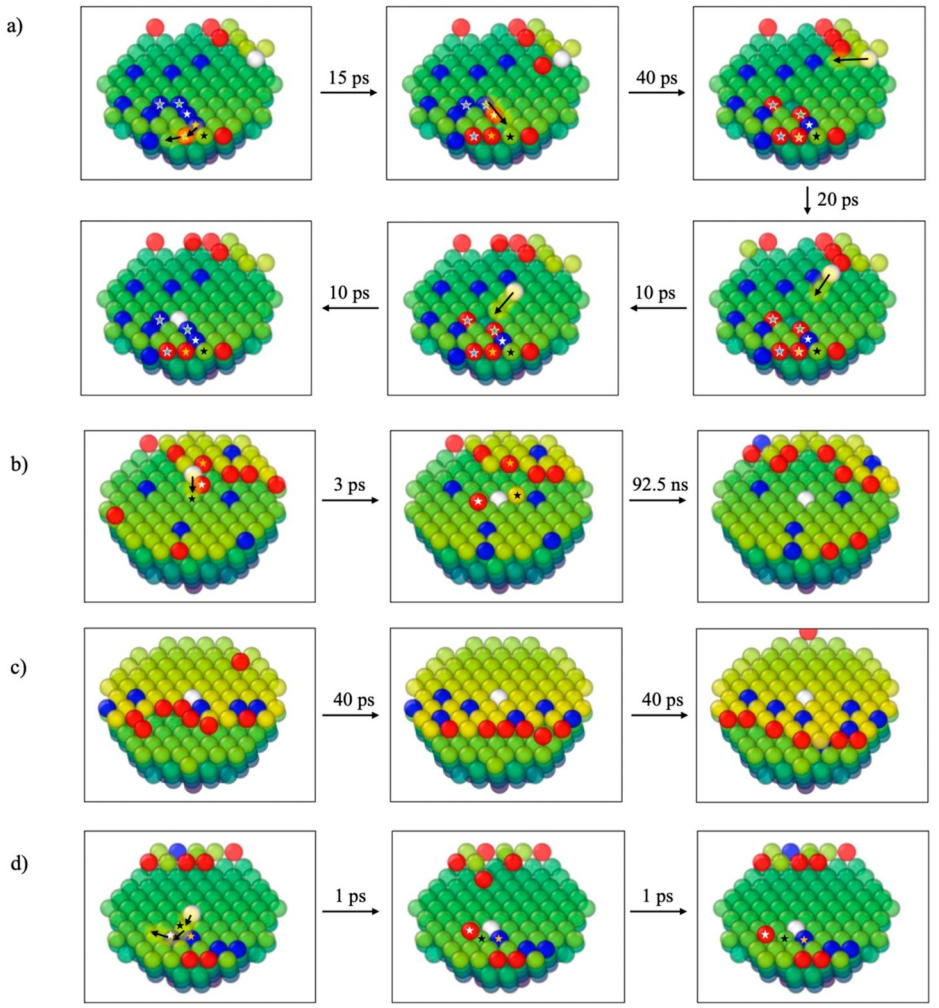

Figure 10. Alloying scheme at the middle terrace. The green to yellow atoms indicate Cu atoms, the red atoms indicates Zn as adatoms, and the blue atoms indicates substituted Zn atoms. The white atom indicate the moving Zn atom. Several atoms are marked with star-shaped symbol to ease the tracking of their positions. (a) Diffusing Zn adatom fills in the vacancy in the middle terrace. (b) Direct exchange between the Zn step adatom and Cu surface atom occurs; then the step adatom moves back, while the substituted Zn atom stays. (c) Deep confinement of Zn atoms by other step adatoms. (d) Indirect exchange at the middle terrace.

the case of the straight edge, the barriers for Cu pop out (event no. 9 in Table S1) and Zn pop out (event no. 10 in table S1) from the lower terrace are very high: 1.61 and 1.19 eV, respectively. However, in the presence of the kinked edge, such barriers are significantly reduced to 1.05 and 0.84 eV for Cu (event no. A13 in Table S1) and Zn (event no. A14 in Table S1), respectively. This indicates the positive contribution of kink sites toward vacancy generations at the lower terrace, mainly by stabilizing the final state of the popped atom. In addition, we found that the Cu or Zn atom nearby other substituted Zn atoms has a smaller pop out barrier to overcome. In the presence of two neighboring Zn atoms, the Cu and Zn pop out barriers (no. A21 and event no. A22 in Table S1) are reduced to 0.93 and 0.64 eV, respectively.

3.3.2.3. Indirect Exchange. In this scheme, the Zn adatom influences the surface atom underneath to push the adjacent surface atom out of the surface (Figure 9c). This scheme involves three atoms: one "initiator" adatom and two "passive" surface atoms. To estimate the barrier of this scheme, we performed DFT calculations using a simplified structure as presented in Table S4. Treating the diffusing adatom as the initiator and one pre-substituted Zn atom at the lower terrace, we found the activation energies to be 0.67 and 1.20 eV for forward (event no. 7 in Table S4) and reverse (event no. D8 in Table S4) processes, respectively.

By observing 60 alloying events at the lower terrace within 5 μs MD simulation, we found the percentages of the first, second, and third schemes to be 74, 22, and 5%, respectively. We also note that the scheme of step-assisted direct exchange and vacancy insertion at the lower terrace might have high similarity when the vacancy is formed near the active atom. Thus, we distinguished these schemes by the lifetime of the vacancy: if the lifetime of the vacancy is within 1 ps, we classified the scheme to step-assisted direct exchange; otherwise, we classified the scheme to vacancy insertion at the lower terrace. In addition, we also found that the incorporated atom at the lower terrace is buried by the fluctuating step adatoms and thus transformed into a subsurface atom for a certain time period (Figure 9d).

3.3.3. Alloying at the Middle Terrace. The homogeneous substitution of Zn into the Cu surface after annealing at 560 K was reported by Sano et al. by means of STM observation.[22] We have performed the MD simulation for up to several μs, but unfortunately, we could not reproduce such homogeneous substitutions due to the slow process of the alloying. Even so, we

https://doi.org/10.1021/acsphyschemau.2c00017
ACS Phys. Chem Au 2022, 2, 430−447

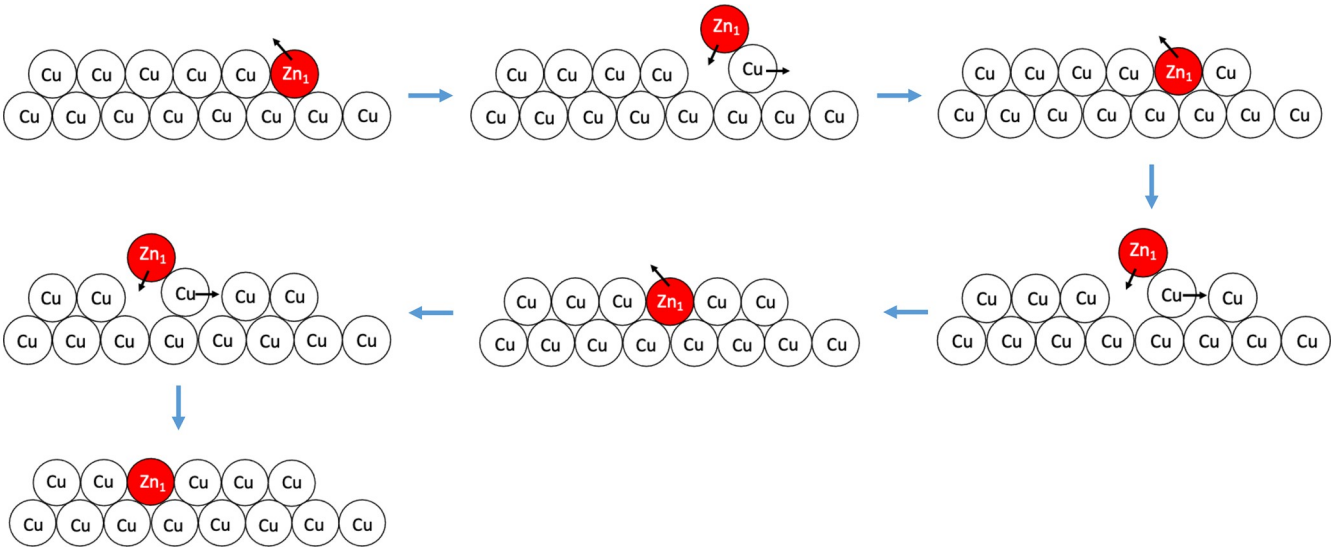

Figure 11. Transformation of Zn step adatoms into incorporated Zn atoms at the middle terrace by means of the local-exchange mechanism. The white and red circles indicate the Cu and Zn atoms, respectively.

still observed a few incorporations of Zn atoms at the middle terrace and investigated the responsible scheme of the alloying. We found that there are four schemes that contribute to the alloying at the middle terrace: (i) vacancy insertion at the middle terrace, (ii) wave deposition mechanism, (iii) confinement by other step adatoms, and (iv) indirect exchange. The characteristics of these schemes are described as follows.

3.3.3.1. Vacancy Insertion at the Middle Terrace. This scheme is similar to the other schemes of vacancy insertion at the upper and lower terraces, except that the vacancy is found at the middle terrace (Figure 10a). The DFT calculations indicate that the vacancy formation by atom hopping at the middle terrace has very high barriers: 2.02 and 1.74 eV for Cu pop out (event no. A1 in Table S1) and Zn pop out (event no. A2 in Table S1), respectively. Therefore, the vacancy found in the middle terrace may result from the lower and upper terraces at which the vacancy generation is easier (event no. A5, A6, A9, A10, A13, and A14 in Table S1).

3.3.3.2. Wave Deposition Mechanism. In this scheme, the Zn atom was originally formed at the lower terrace through the step-assisted direct exchange or vacancy insertion at the lower terrace. However, at a later time, the step or kink sites which previously assisted the mechanism disappear due to the step fluctuation, leaving the Zn atom incorporated at the middle terrace (Figure 10b). Thus, the step fluctuation acts like a wave which moves back and forth, similar to the behavior of the sea wave that deposits the material at the sea shore.

3.3.3.3. Confinement by Other Step Adatoms. This scheme is similar to the confinement of Zn step adatoms at the upper terrace, except that in this case, the Zn adatoms are confined deeper to the terrace (Figure 10c).

3.3.3.4. Indirect Exchange. The last scheme is the indirect-exchange mechanism, which is similar to the one occurring at the lower terrace (Figure 10d). Using a simplified structure, the DFT activation energy is calculated to be 1.07 eV (event no. D4 in Table S4). In the case of no pre-substituted Zn, the activation energy is increased to 1.39 eV (event no. D1 in Table S4), indicating the role of pre-substituted Zn in the process to lower the activation energy by ∼0.3 eV.

Based on observation of 46 alloying events at the middle terrace, the percentages for the first, second, third, and fourth schemes are found to be 13, 39, 33, and 15%, respectively. Even though the alloying scheme at the middle terrace is dominated by the second and third schemes, the incorporated Zn atoms resulting from this scheme are close to the step edge and can easily transform back to step adatoms due to the high intensity of the step fluctuation. On the other hand, the incorporated Zn atoms farther from the step edge are more stable and stay incorporated longer.

3.3.4. Complete Scenario of Cu−Zn Surface Alloying and Comparison with STM Observation. Summarizing all the alloying schemes that we found, we then devise the Cu−Zn surface alloying based on our simulation. Initially, the randomly deposited Zn atoms will localize at the step edge. At room temperature, the Zn islands might be formed through bindings between Zn adatoms on the terrace (Figure 5c). However, such islands are not stable and readily collapse when the temperature is increased to 550 K. Most of the Zn atoms then attach to the step edge or diffuse as adatoms on the terrace (Figure 6a). At 700 K, the alloying at the upper terrace occurs, mainly due to confinement of Zn by other step adatoms and the exchange descend of diffusing Zn adatoms on the upper terrace. The alloying at the lower terrace occurs slightly later than the alloying at the upper terrace. The main mechanism of the alloying at this region is the direct exchange between the Zn step adatom and surface atom underneath. Finally, the alloying at the middle terrace occurs at a later stage, in which the main mechanism is found to be wave deposition and deep confinement by the other step adatoms. We noted that the Zn alloyed at the middle and lower terraces has not been included in the previous DFT studies of the methanol synthesis by CO_2 hydrogenation on Cu−Zn surface results.[8,11,13,18,19] In such catalytic reaction, it was suggested that Zn stabilizes the adsorbates that bind through O atoms and destabilizes the ones that bind through C atoms. Thus, the presence of Zn atoms at the lower and middle terraces may also affect the catalytic reactions to some extent. The surface alloying is also accompanied by the formation of a wavy step edge with a high kink density, much different from the model of rigid step edge used in the previous DFT studies.

The possible mechanism for the alloy formation has also been proposed based on previous STM observation.[22] Since it was observed that Zn incorporates the surface from the step into the

https://doi.org/10.1021/acsphyschemau.2c00017
ACS Phys. Chem Au 2022, 2, 430−447

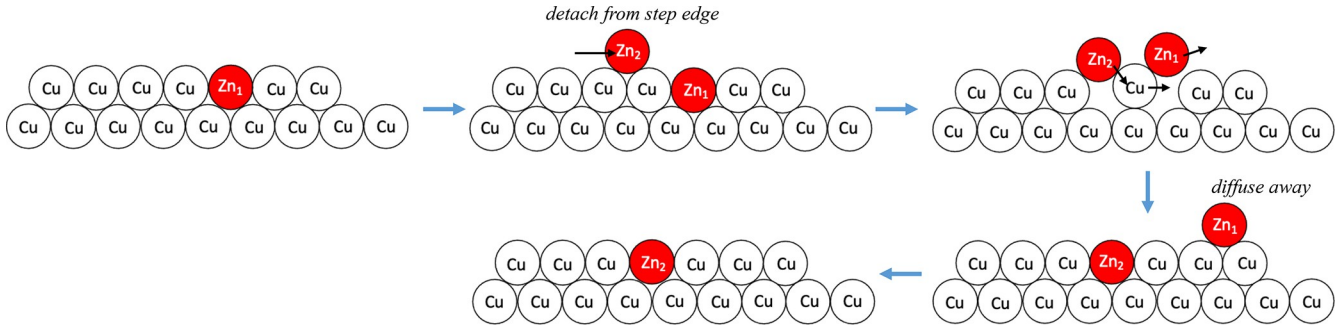

Figure 12. Migration of incorporated Zn at the middle terrace by means of the indirect-exchange mechanism. The white and red circles indicate the Cu and Zn atoms respectively.

terrace without long-distance Zn migration, it was suggested that the alloying mechanism occurs through the so-called local exchange between Zn and the neighboring Cu atoms (Figure 11). This mechanism is initiated by hopping ascend of Zn step adatoms, followed by Zn exchange descend. Once the Zn atom is incorporated at the upper terrace, the Zn atom then performs the sequence of pop out and exchange descend mechanisms to propagate to the middle terrace. In the case of alloying at the upper terrace, the local-exchange mechanisms were also found in our simulation in the form of the sequence of hopping ascend and exchange descend as mentioned in the previous subsection. However, we could not find such mechanisms in operation to form the alloy at the middle terrace or the region far from the edge. In addition, by performing the DFT calculations using a simplified structure, we found that the local exchange has a barrier of more than 2 eV (events F1 and F2 in Table S6) at the middle terrace. Therefore, we consider that such mechanisms are unlikely to be responsible for the alloying at the middle terrace or any part of the surface which is far from the step edge.

Interestingly, a kind of propagation of Zn atoms from upper and lower terraces to middle terraces is found in our simulation, which is achieved through the indirect exchange as discussed in the previous section. Such a propagation is essentially different from the one suggested by Sano et al. since in the case of the indirect-exchange mechanism, the Zn at the initial and final states is a different atom. In addition, our finding of the indirect-exchange mechanism requires the diffusing Zn terrace adatom, which mainly comes from the detachment of the Zn step adatom (Figure 12).

It was reported that the long jump of Zn atoms was not observed in previous STM observation; thus, the migration of Zn-incorporated atoms occurs locally in the form of short propagation. Considering the moderate barrier of adatom formation by detachment or the step climbing of Zn step adatoms, we think that the Zn adatom diffusing on the terrace should exist in the experiment. To investigate this idea, we calculated the histogram of the adatom's lifetime based on our simulation as shown in Figure 13. The histogram shows that the majority of adatoms have a very short lifetime, with 0.5 ns at the longest. By fitting the exponential function to the histogram, we obtained a very short time constant (τ) of 34.498 ps. Given the low frequency of adatoms with a long lifetime, it is very reasonable that they are invisible in the experiment. The reason behind the apparent short propagation of Zn-incorporated atoms observed in the experiment is that the pre-substituted Zn atom contributes in lowering the barrier of the indirect exchange as shown in events D3 and D4 in Table S4. Therefore, the indirect-exchange mechanism would tend to happen nearby

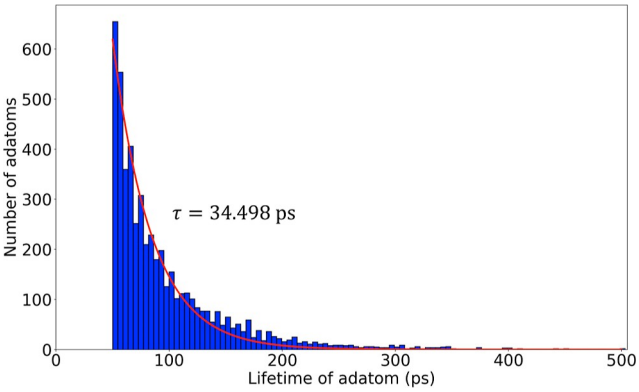

Figure 13. Histogram of the lifetime of adatoms found in the simulation.

another incorporated Zn atom, which in the experiment might be considered as short or local propagation.

Before attempting to revise the possible scenario of the Cu−Zn surface alloying, we would like to highlight an important difference between our simulation and actual experiment. Naturally, the Zn atom must overcome the barrier to climb the step edge (i.e., hopping-ascend or exchange-ascend barrier). However, due to the periodic boundary condition employed in our simulation, the Zn atoms that were in the bottom-most terrace can go directly to the top-most terrace just by crossing the boundary of the unit cell. Such circumstances would result in the constant presence of Zn atoms diffusing on the higher terrace as long as they have not been incorporated to the surface. This is obviously not the case in the experiment. Therefore, given the condition where the number of diffusing Zn adatoms on the higher terrace is limited, the source of adatoms in the experiment would come mainly through hopping ascend or exchange ascend of Zn step adatoms.

3.4. Migration Rates and Activation Energy

We estimated the Zn migration rate $\nu(s^{-1})$ at constant temperature by using the Poisson statistics[22,63]

$$\frac{n(t)}{n_0} = \exp(-\nu t) \qquad \text{or } \ln\left(\frac{n(t)}{n_0}\right) = -\nu t$$

where $n(t)/n_0$ is the fraction of Zn atoms that had not moved within a time interval t. The migration rate is thus obtained by plotting the logarithm of $n(t)/n_0$ against the time interval t and then taking the slope. The resulting Poisson statistics of Zn migrations at 550, 700, and 1000 K are shown in Figure 14a−c. At each temperature, the resulting migration rate is expressed as

https://doi.org/10.1021/acsphyschemau.2c00017
ACS Phys. Chem Au 2022, 2, 430−447

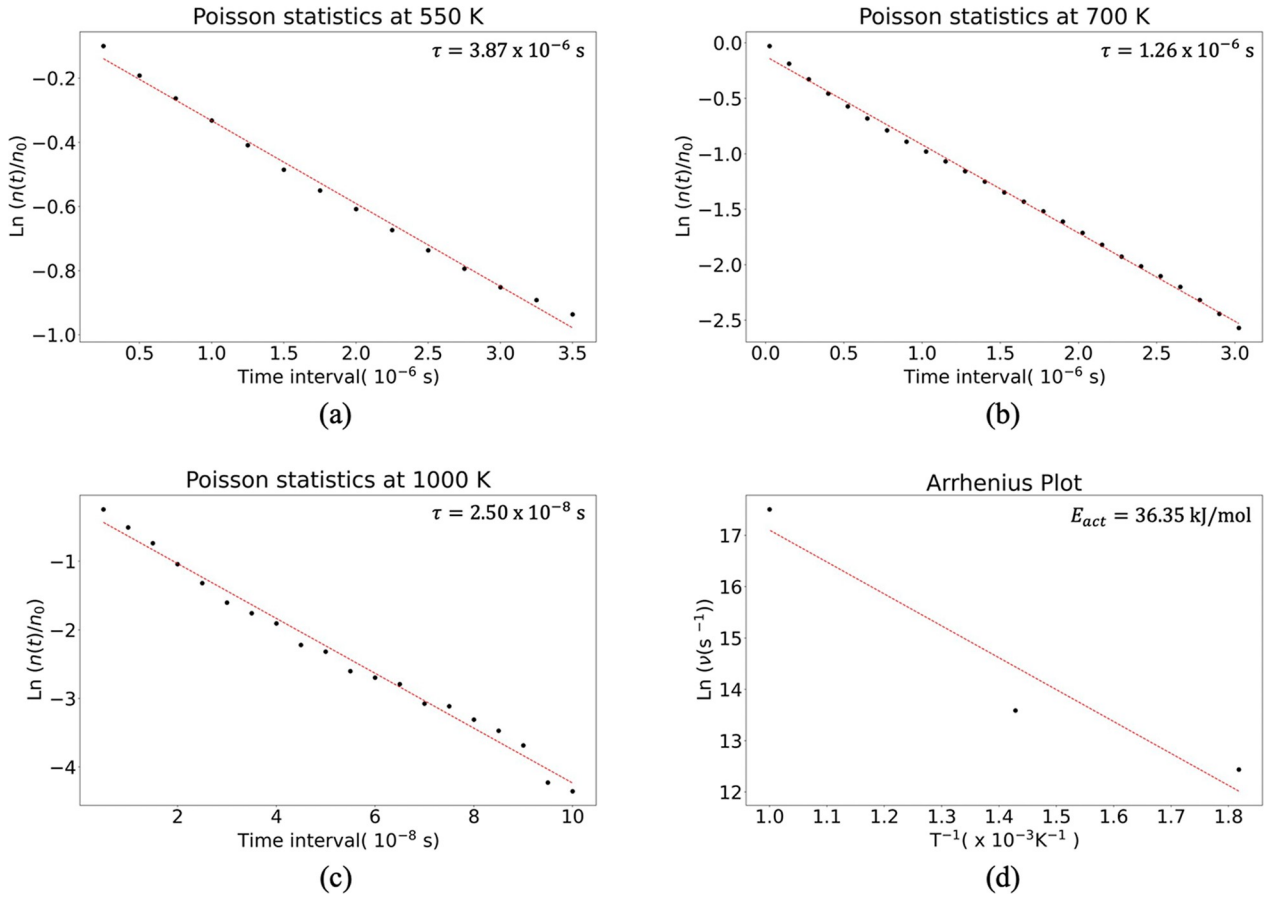

Figure 14. Poisson statistics at (a) 550, (b) 700, and (c) 1000 K. The poisson statistic is used to estimate the Zn migration rate (i.e., the inverse of the residence time τ). (d) The Arrhenius plot to estimate activation energy of Zn migration based on the migration rate at different temperatures.

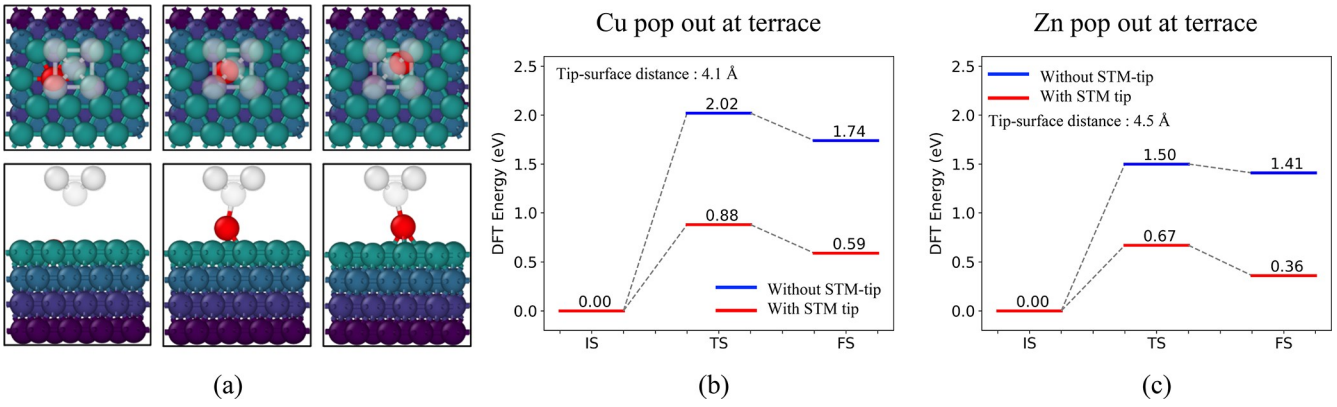

Figure 15. (a) The mechanism of the atomic pop out assisted by STM tip (left to right). The energetics of this event for Cu pop out and Zn pop out at the terrace are shown in (b) and (c), respectively.

the average residence time τ (s), which equals to the inverse of the migration rate. The residence times for temperatures of 550, 700, and 1000 K are calculated to be 3.87 μs, 1.26 μs, and 25 ns, respectively. By using the Arrhenius law, we thus estimated the activation energy of the Zn migrations to be 0.52 eV. The Arrhenius plot is shown in Figure 14d.

Based on STM observation, Sano et al. have derived the activation energy to be 0.25 eV,[22] which is much lower than our calculation. One possible origin of this discrepancy is the influence of the STM tip used in the simulation. It has been reported that the STM tip can induce motion of adatoms, enhance the vacancy formation, and even move the embedded atom.[64−67] To give more details to this, we calculated simple elementary events under the influence of the STM tip and measured the change of the barriers due to the influence of the tip. The tip is modelled as the isolated (100) surface of tungsten, a similar element to the tip used in the previous STM measurements.[22] The details of the model and calculation can be found in section S4 of the Supporting Information.

As discussed in the previous section, the barriers of Cu pop out and Zn pop out without the influence of the tip are 2.02 and 1.50 eV, respectively. Interestingly, we found that these barriers of pop out are reduced significantly under the STM tip to 0.88 eV (the tip−surface distance is 4.1 Å) and 0.67 eV (the tip−

https://doi.org/10.1021/acsphyschemau.2c00017
ACS Phys. Chem Au 2022, 2, 430−447

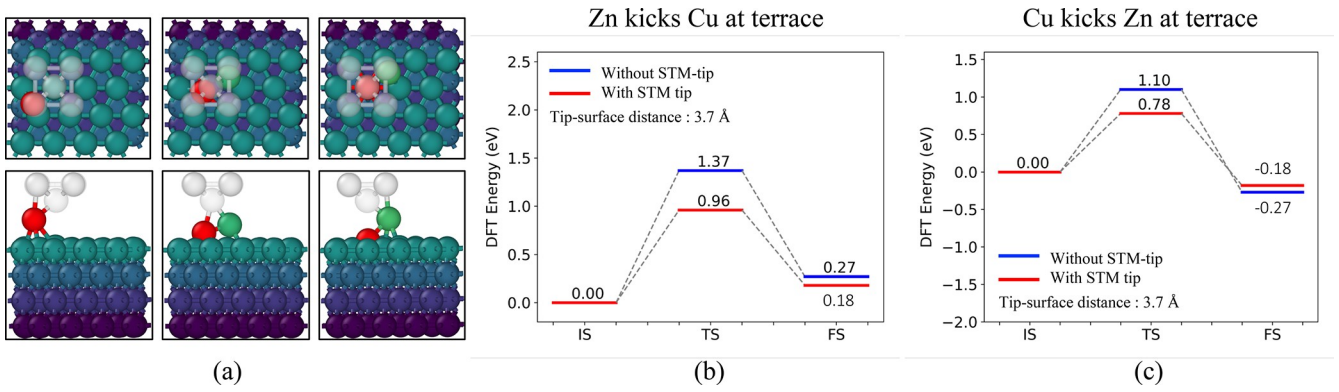

Figure 16. (a) The mechanism of the direct exchange assisted by STM tip. From left to right is the mechanism of Zn adatom to kick out the Cu surface atom. From right to left is the mechanism of Cu adatom to kick out the Zn surface atom. The energetics of both event are shown in (b) and (c).

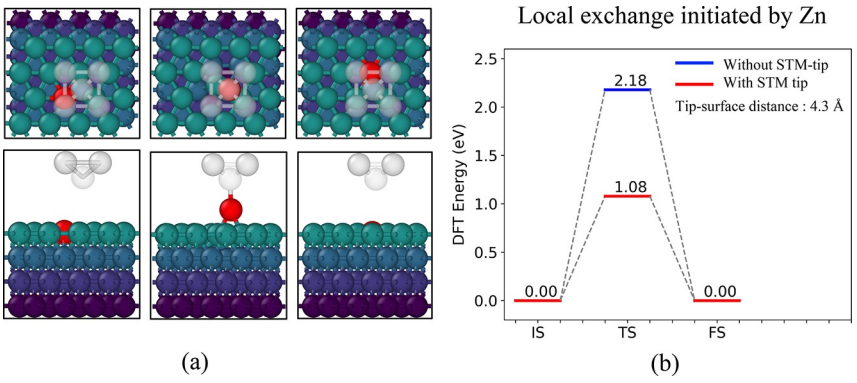

Figure 17. (a) The mechanism of hypotetical local exchange initiated by Zn pop out under influence of the STM tip. (b) The energetic of the event.

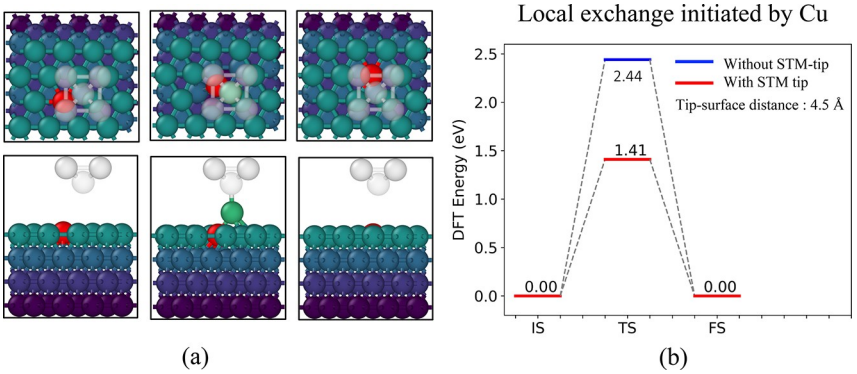

Figure 18. (a) The mechanism of hypotetical local exchange initiated by Cu pop out under influence of the STM tip. (b) The energetic of the event.

surface distance is 4.5 Å) for Cu and Zn, respectively (Figure 15). In the case of direct exchange between Zn and Cu atoms, the barrier for Zn adatom to kick out Cu surface atom is reduced from 1.37 to 0.96 eV and the barrier for Cu adatom to kick Zn surface atom is reduced from 1.10 to 0.78 eV with a tip−surface distance of 3.7 Å (Figure 16). In addition, we found a very large reduction of around 1 eV for the barrier of hypothetical local exchange under the STM tip. In the case of local exchange initiated by Zn pop out (with a tip−surface distance of 4.3 Å), the barrier is reduced from 2.18 to 1.08 eV (Figure 17). Similarly, the barrier of local exchange initiated by Cu pop out (with a tip distance of 4.5 Å) is also reduced from 2.44 to 1.41 eV (Figure 18). This suggests that the STM tip may accelerate the alloying at the middle terrace by assisting vacancy formation and direct exchange between Zn and Cu. Under the influence of the STM tip, the local exchange might also be possible as a rare process given the significant reduction in the barrier. More detailed study on the alloying mechanisms under the influence of the STM tip will be the topic for further studies.

4. CONCLUSIONS

In the present study, we investigated the structure and formation process of the Cu−Zn surface alloy on Cu(997) by machine-learning MD. GP regression aided with the on-the-fly learning scheme was employed to build the force field based on data of first-principles calculations. The resulting force field is validated by comparing the DFT- and GP-calculated barriers of various elementary events, the atomic forces of the TS structures, and the forces of the atomic environments with the highest uncertainty found during simulation.

https://doi.org/10.1021/acsphyschemau.2c00017
ACS Phys. Chem Au 2022, 2, 430−447

The simulation reveals atomistic details of the alloying process, that is, the incorporation of deposited Zn adatoms to the Cu substrate. We found that Zn incorporates the surface not only at the upper terrace but also at lower and middle terraces which have not been considered in the previous DFT studies of methanol synthesis on the Cu−Zn surface. The surface alloying is also accompanied by the formation of a wavy step edge with a high kink density, much different from the model of rigid step edge used in the previous DFT studies. By calculating the barrier of elementary events of step edge fluctuations (i.e., attachment and detachment of adatoms to/from the step edge), we found that all the elementary events involving Zn atoms have a lower barrier than the pure Cu system, suggesting that Zn atoms enhance the step edge fluctuations.

The time evolution of the surface shows that the alloying is initiated at upper and lower terraces near the step edge, giving emphasis to the role of steps and kinks in the surface alloying which lower the barriers of elementary events such as vacancy generation and direct exchange. The alloyed Zn was found at the middle terrace at the later stage of the simulation. We found that the alloying at the upper terrace is dominated by the confinement of Zn step adatoms by other step adatoms which migrate heavily along the step edge, highlighting the importance of step fluctuation in the alloying which is also enhanced by the presence of Zn. Meanwhile, the alloying at the lower terrace is dominated by the direct exchange between the Zn step adatom and the Cu surface atom underneath. In the case of alloying at the middle terrace, the alloying is dominated by the wave deposition and deep confinement of Zn adatoms.

The short propagation of alloyed Zn in the middle terrace was observed to occur by means of the indirect-exchange mechanism instead of local exchange as proposed in the previous STM observation. The comparison of migration rate and activation energies to the result of STM observation is also made. Based on Arrhenius plots, we calculated the activation energy to be 0.52 eV, which is around 2 times higher than the experimental activation energy measured by experiments. We explained such discrepancy as the result of the STM tip influence on the surface. In addition, we have found that at a certain distance from the surface, the STM tip significantly affects the elementary events such as vacancy formation and direct exchange.

■ ASSOCIATED CONTENT

Supporting Information

The Supporting Information is available free of charge at https://pubs.acs.org/doi/10.1021/acsphyschemau.2c00017.

Calculation of surface energy, details on active and on-the-fly learning schemes, energetics of elementary events, and details on STM tip dependency (PDF)

The short videos showing the MD snapshots and alloying mechanisms at upper, middle, and lower terraces (ZIP)

■ AUTHOR INFORMATION

Corresponding Author

Yoshitada Morikawa − *Department of Precision Engineering, Graduate School of Engineering, Osaka University, Suita, Osaka 565-0871, Japan; Elements Strategy Initiative for Catalysts and Batteries (ESICB), Kyoto University, Kyoto 615-8245, Japan; Research Center for Precision Engineering, Graduate School of Engineering, Osaka University, Suita, Osaka 565-0871, Japan;* orcid.org/0000-0003-4895-4121; Email: morikawa@prec.eng.osaka-u.ac.jp

Author

Harry H. Halim − *Department of Precision Engineering, Graduate School of Engineering, Osaka University, Suita, Osaka 565-0871, Japan;* orcid.org/0000-0001-6285-1650

Complete contact information is available at: https://pubs.acs.org/10.1021/acsphyschemau.2c00017

Notes

The authors declare no competing financial interest.

The MGP force-field that we used in this study are available under the following DOI: 10.24435/materialscloud:gh-wt in the Materials Cloud archive.[68]

■ ACKNOWLEDGMENTS

H.H.H. would like to thank the scholarship aid in Graduate School of Engineering, Osaka University, provided by MEXT (Ministry of Education, Culture, Sports, Science, and Technology). This research was partly supported by a Grant-in-Aid for Transformative Research Areas (A) "Hyper-Ordered Structure Science" (grant no. JP20H05883) and Grant-in-Aid for Scientific Research (B) (grant no. JP20H02569) from the Japan Society for the Promotion of Science (JSPS) and by JST SICORP, Japan (grant no. JPMJSC21E4). The numerical calculations were performed using computer resources at the Institute for Solid State Physics, University of Tokyo.

■ REFERENCES

(1) Groß, A. Reactivity of Bimetallic Systems Studied from First Principles. *Top. Catal.* **2006**, *37*, 29−39.

(2) Chen, J. G.; Menning, C. A.; Zellner, M. B. Monolayer Bimetallic Surfaces: Experimental and Theoretical Studies of Trends in Electronic and Chemical Properties. *Surf. Sci. Rep.* **2008**, *63*, 201−254.

(3) Knudsen, J.; Nilekar, A. U.; Vang, R. T.; Schnadt, J.; Kunkes, E. L.; Dumesic, J. A.; Mavrikakis, M.; Besenbacher, F. A Cu/Pt Near-Surface Alloy for Water−Gas Shift Catalysis. *J. Am. Chem. Soc.* **2007**, *129*, 6485−6490.

(4) Wang, C.; Markovic, N. M.; Stamenkovic, V. R. Advanced Platinum Alloy Electrocatalysts for the Oxygen Reduction Reaction. *ACS Catal.* **2012**, *2*, 891−898.

(5) Fan, J.; Du, H.; Zhao, Y.; Wang, Q.; Liu, Y.; Li, D.; Feng, J. Recent Progress on Rational Design of Bimetallic Pd Based Catalysts and Their Advanced Catalysis. *ACS Catal.* **2020**, *10*, 13560−13583.

(6) Zhang, Y.-C.; Han, C.; Gao, J.; Pan, L.; Wu, J.; Zhu, X.-D.; Zou, J.-J. NiCo-Based Electrocatalysts for the Alkaline Oxygen Evolution Reaction: A Review. *ACS Catal.* **2021**, *11*, 12485−12509.

(7) Fujitani, T.; Nakamura, I.; Uchijima, T.; Nakamura, J. The Kinetics and Mechanism of Methanol Synthesis by Hydrogenation of CO2 over a Zn-Deposited Cu(111) Surface. *Surf. Sci.* **1997**, *383*, 285−298.

(8) Behrens, M.; Studt, F.; Kasatkin, I.; Kühl, S.; Hävecker, M.; Abild-Pedersen, F.; Zander, S.; Girgsdies, F.; Kurr, P.; Kniep, B.-L.; Tovar, M.; Fischer, R. W.; Nørskov, J. K.; Schlögl, R. The Active Site of Methanol Synthesis over Cu/ZnO/Al2O3 Industrial Catalysts. *Science* **2012**, *336*, 893.

(9) Fujitani, T.; Nakamura, J. The Chemical Modification Seen in the Cu/ZnO Methanol Synthesis Catalysts. *Appl. Catal. Gen.* **2000**, *191*, 111−129.

(10) Porosoff, M. D.; Yan, B.; Chen, J. G. Catalytic Reduction of CO2 by H2 for Synthesis of CO, Methanol and Hydrocarbons: Challenges and Opportunities. *Energy Environ. Sci.* **2016**, *9*, 62−73.

(11) Studt, F.; Behrens, M.; Kunkes, E. L.; Thomas, N.; Zander, S.; Tarasov, A.; Schumann, J.; Frei, E.; Varley, J. B.; Abild-Pedersen, F.; Nørskov, J. K.; Schlögl, R. The Mechanism of CO and CO2

Hydrogenation to Methanol over Cu-Based Catalysts. *ChemCatChem* **2015**, *7*, 1105−1111.
(12) Nakamura, J.; Choi, Y.; Fujitani, T. On the Issue of the Active Site and the Role of ZnO in Cu/ZnO Methanol Synthesis Catalysts. *Top. Catal.* **2003**, *22*, 277−285.
(13) Kattel, S.; Ramírez, P. J.; Chen, J. G.; Rodriguez, J. A.; Liu, P. Active Sites for CO2 Hydrogenation to Methanol on Cu/ZnO Catalysts. *Science* **2017**, *355*, 1296.
(14) Nakamura, J.; Fujitani, T.; Kuld, S.; Helveg, S.; Chorkendorff, I.; Sehested, J. Comment on "Active Sites for CO2 Hydrogenation to Methanol on Cu/ZnO Catalysts. *Science* **2017**, *357*, No. eaan8074.
(15) Kattel, S.; Ramírez, P. J.; Chen, J. G.; Rodriguez, J. A.; Liu, P. Response to Comment on "Active Sites for CO2 Hydrogenation to Methanol on Cu/ZnO Catalysts. *Science* **2017**, *357*, No. eaan8210.
(16) Holse, C.; Elkjær, C. F.; Nierhoff, A.; Sehested, J.; Chorkendorff, I.; Helveg, S.; Nielsen, J. H. Dynamic Behavior of CuZn Nanoparticles under Oxidizing and Reducing Conditions. *J. Phys. Chem. C* **2015**, *119*, 2804−2812.
(17) Zabilskiy, M.; Sushkevich, V. L.; Palagin, D.; Newton, M. A.; Krumeich, F.; van Bokhoven, J. A. The Unique Interplay between Copper and Zinc during Catalytic Carbon Dioxide Hydrogenation to Methanol. *Nat. Commun.* **2020**, *11*, 2409.
(18) Wang, S.-S.; Su, H.-Y.; Gu, X.-K.; Li, W.-X. Differentiating Intrinsic Reactivity of Copper, Copper−Zinc Alloy, and Copper/Zinc Oxide Interface for Methanol Steam Reforming by First-Principles Theory. *J. Phys. Chem. C* **2017**, *121*, 21553−21559.
(19) Wang, S.-s.; Jian, M.-z.; Su, H.-y.; Li, W.-x. First-Principles Microkinetic Study of Methanol Synthesis on Cu(221) and ZnCu(221) Surfaces. *Chin. J. Chem. Phys.* **2018**, *31*, 284−290.
(20) Yoshihara, J.; Campbell, C. T. Methanol Synthesis and Reverse Water−Gas Shift Kinetics over Cu(110) Model Catalysts: Structural Sensitivity. *J. Catal.* **1996**, *161*, 776−782.
(21) van Rensburg, W. J.; Petersen, M. A.; Datt, M. S.; van den Berg, J.-A.; van Helden, P. On the Kinetic Interpretation of DFT-Derived Energy Profiles: Cu-Catalyzed Methanol Synthesis. *Catal. Lett.* **2015**, *145*, 559−568.
(22) Sano, M.; Adaniya, T.; Fujitani, T.; Nakamura, J. Formation Process of a Cu−Zn Surface Alloy on Cu(111) Investigated by Scanning Tunneling Microscopy. *J. Phys. Chem. B* **2002**, *106*, 7627−7633.
(23) Giesen, M.; Icking-Konert, G. S. Equilibrium Fluctuations and Decay of Step Bumps on Vicinal Cu (111) Surfaces. *Surf. Sci.* **1998**, *412*−*413*, 645−656.
(24) Giesen, M. Step and Island Dynamics at Solid/Vacuum and Solid/Liquid Interfaces. *Prog. Surf. Sci.* **2001**, *68*, 1−154.
(25) Eren, B.; Zherebetskyy, D.; Patera, L. L.; Wu, C. H.; Bluhm, H.; Africh, C.; Wang, L.-W.; Somorjai, G. A.; Salmeron, M. Activation of Cu(111) Surface by Decomposition into Nanoclusters Driven by CO Adsorption. *Science* **2016**, *351*, 475.
(26) Michalka, J. R.; Latham, A. P.; Gezelter, J. D. CO-Induced Restructuring on Stepped Pt Surfaces: A Molecular Dynamics Study. *J. Phys. Chem. C* **2016**, *120*, 18180−18190.
(27) Tang, M.; Yuan, W.; Ou, Y.; Li, G.; You, R.; Li, S.; Yang, H.; Zhang, Z.; Wang, Y. Recent Progresses on Structural Reconstruction of Nanosized Metal Catalysts via Controlled-Atmosphere Transmission Electron Microscopy: A Review. *ACS Catal.* **2020**, *10*, 14419−14450.
(28) Meng, J.; Zhu, B.; Gao, Y. Structure Reconstruction of Metal/Alloy in Reaction Conditions: A Volcano Curve? *Faraday Discuss.* **2021**, *229*, 62−74.
(29) Dong, Z.; Liu, W.; Zhang, L.; Wang, S.; Luo, L. Structural Evolution of Cu/ZnO Catalysts during Water-Gas Shift Reaction: An In Situ Transmission Electron Microscopy Study. *ACS Appl. Mater. Interfaces* **2021**, *13*, 41707−41714.
(30) Vogt, C.; Meirer, F.; Monai, M.; Groeneveld, E.; Ferri, D.; van Santen, R. A.; Nachtegaal, M.; Unocic, R. R.; Frenkel, A. I.; Weckhuysen, B. M. Dynamic Restructuring of Supported Metal Nanoparticles and Its Implications for Structure Insensitive Catalysis. *Nat. Commun.* **2021**, *12*, 7096.
(31) Behler, J. Four Generations of High-Dimensional Neural Network Potentials. *Chem. Rev.* **2021**, *121*, 10037−10072.
(32) Artrith, N.; Hiller, B.; Behler, J. Neural Network Potentials for Metals and Oxides − First Applications to Copper Clusters at Zinc Oxide. *Phys. Status Solidi B* **2013**, *250*, 1191−1203.
(33) Elias, J. S.; Artrith, N.; Bugnet, M.; Giordano, L.; Botton, G. A.; Kolpak, A. M.; Shao-Horn, Y. Elucidating the Nature of the Active Phase in Copper/Ceria Catalysts for CO Oxidation. *ACS Catal.* **2016**, *6*, 1675−1679.
(34) Weinreich, J.; Römer, A.; Paleico, M. L.; Behler, J. Properties of α-Brass Nanoparticles. 1. Neural Network Potential Energy Surface. *J. Phys. Chem. C* **2020**, *124*, 12682−12695.
(35) Weinreich, J.; Paleico, M. L.; Behler, J. Properties of α-Brass Nanoparticles II: Structure and Composition. *J. Phys. Chem. C* **2021**, *125*, 14897−14909.
(36) Jinnouchi, R.; Miwa, K.; Karsai, F.; Kresse, G.; Asahi, R. On-the-Fly Active Learning of Interatomic Potentials for Large-Scale Atomistic Simulations. *J. Phys. Chem. Lett.* **2020**, *11*, 6946−6955.
(37) Shang, C.; Zhang, X.-J.; Liu, Z.-P. Stochastic Surface Walking Method for Crystal Structure and Phase Transition Pathway Prediction. *Phys. Chem. Chem. Phys.* **2014**, *16*, 17845−17856.
(38) Zhang, X.-J.; Shang, C.; Liu, Z.-P. Stochastic Surface Walking Reaction Sampling for Resolving Heterogeneous Catalytic Reaction Network: A Revisit to the Mechanism of Water-Gas Shift Reaction on Cu. *J. Chem. Phys.* **2017**, *147*, 152706.
(39) Ma, S.; Shang, C.; Liu, Z.-P. Heterogeneous Catalysis from Structure to Activity via SSW-NN Method. *J. Chem. Phys.* **2019**, *151*, 050901.
(40) Schran, C.; Brezina, K.; Marsalek, O. Committee Neural Network Potentials Control Generalization Errors and Enable Active Learning. *J. Chem. Phys.* **2020**, *153*, 104105.
(41) Jinnouchi, R.; Karsai, F.; Kresse, G. On-the-Fly Machine Learning Force Field Generation: Application to Melting Points. *Phys. Rev. B: Condens. Matter Mater. Phys.* **2019**, *100*, 014105.
(42) Jinnouchi, R.; Lahnsteiner, J.; Karsai, F.; Kresse, G.; Bokdam, M. Phase Transitions of Hybrid Perovskites Simulated by Machine-Learning Force Fields Trained on the Fly with Bayesian Inference. *Phys. Rev. Lett.* **2019**, *122*, 225701.
(43) Vandermause, J.; Torrisi, S. B.; Batzner, S.; Xie, Y.; Sun, L.; Kolpak, A. M.; Kozinsky, B. On-the-Fly Active Learning of Interpretable Bayesian Force Fields for Atomistic Rare Events. *npj Comput. Mater.* **2020**, *6*, 20.
(44) Lim, J. S.; Molinari, N.; Duanmu, K.; Sautet, P.; Kozinsky, B. Automated Detection and Characterization of Surface Restructuring Events in Bimetallic Catalysts. *J. Phys. Chem. C* **2019**, *123*, 16332−16344.
(45) Lim, J. S.; Vandermause, J.; van Spronsen, M. A.; Musaelian, A.; Xie, Y.; Sun, L.; O'Connor, C. R.; Egle, T.; Molinari, N.; Florian, J.; Duanmu, K.; Madix, R. J.; Sautet, P.; Friend, C. M.; Kozinsky, B. Evolution of Metastable Structures at Bimetallic Surfaces from Microscopy and Machine-Learning Molecular Dynamics. *J. Am. Chem. Soc.* **2020**, *142*, 15907−15916.
(46) Morikawa, Y.; Ishii, H.; Seki, K. Theoretical Study of N-Alkane Adsorption on Metal Surfaces. *Phys. Rev. B: Condens. Matter Mater. Phys.* **2004**, *69*, 041403.
(47) Morikawa, Y.; Iwata, K.; Terakura, K. Theoretical Study of Hydrogenation Process of Formate on Clean and Zn Deposited Cu(111) Surfaces. *Appl. Surf. Sci.* **2001**, *169*−*170*, 11−15.
(48) Vanderbilt, D. Soft Self-Consistent Pseudopotentials in a Generalized Eigenvalue Formalism. *Phys. Rev. B: Condens. Matter Mater. Phys.* **1990**, *41*, 7892−7895.
(49) Klimeš, J.; Bowler, D. R.; Michaelides, A. Van Der Waals Density Functionals Applied to Solids. *Phys. Rev. B: Condens. Matter Mater. Phys.* **2011**, *83*, 195131.
(50) Hamamoto, Y.; Hamada, I.; Inagaki, K.; Morikawa, Y. Self-Consistent van Der Waals Density Functional Study of Benzene Adsorption on Si(100). *Phys. Rev. B: Condens. Matter Mater. Phys.* **2016**, *93*, 245440.

(51) Straumanis, M. E.; Yu, L. S. Lattice Parameters, Densities, Expansion Coefficients and Perfection of Structure of Cu and of Cu−In α Phase. *Acta Crystallogr., Sect. A: Cryst. Phys., Diffr., Theor. Gen. Crystallogr.* **1969**, *25*, 676−682.
(52) de Boer, F. R.; Mattens, W. C. M.; Boom, R.; Miedema, A. R.; Niessen, A. K.*Cohesion in Metals*; North-Holland: Netherlands, 1988; p 662.
(53) Virtanen, P.; Gommers, R.; Oliphant, T. E.; Haberland, M.; Reddy, T.; Cournapeau, D.; Burovski, E.; Peterson, P.; Weckesser, W.; Bright, J.; van der Walt, S. J.; Brett, M.; Wilson, J.; Millman, K. J.; Mayorov, N.; Nelson, A. R. J.; Jones, E.; Kern, R.; Larson, E.; Carey, C. J.; Polat, İ.; Feng, Y.; Moore, E. W.; VanderPlas, J.; Laxalde, D.; Perktold, J.; Cimrman, R.; Henriksen, I.; Quintero, E. A.; Harris, C. R.; Archibald, A. M.; Ribeiro, A. H.; Pedregosa, F.; van Mulbregt, P.; Vijaykumar, A.; Bardelli, A. P.; Rothberg, A.; Hilboll, A.; Kloeckner, A.; Scopatz, A.; Lee, A.; Rokem, A.; Woods, C. N.; Fulton, C.; Masson, C.; Häggström, C.; Fitzgerald, C.; Nicholson, D. A.; Hagen, D. R.; Pasechnik, D. V.; Olivetti, E.; Martin, E.; Wieser, E.; Silva, F.; Lenders, F.; Wilhelm, F.; Young, G.; Price, G. A.; Ingold, G.-L.; Allen, G. E.; Lee, G. R.; Audren, H.; Probst, I.; Dietrich, J. P.; Silterra, J.; Webber, J. T.; Slavič, J.; Nothman, J.; Buchner, J.; Kulick, J.; Schönberger, J. L.; de Miranda Cardoso, J. V.; Reimer, J.; Harrington, J.; Rodríguez, J. L. C.; Nunez-Iglesias, J.; Kuczynski, J.; Tritz, K.; Thoma, M.; Newville, M.; Kümmerer, M.; Bolingbroke, M.; Tartre, M.; Pak, M.; Smith, N. J.; Nowaczyk, N.; Shebanov, N.; Pavlyk, O.; Brodtkorb, P. A.; Lee, P.; McGibbon, R. T.; Feldbauer, R.; Lewis, S.; Tygier, S.; Sievert, S.; Vigna, S.; Peterson, S.; More, S.; Pudlik, T.; Oshima, T.; Pingel, T. J.; Robitaille, T. P.; Spura, T.; Jones, T. R.; Cera, T.; Leslie, T.; Zito, T.; Krauss, T.; Upadhyay, U.; Halchenko, Y. O.; Vázquez-Baeza, Y. SciPy 1.0 Contributors. SciPy 1.0: Fundamental Algorithms for Scientific Computing in Python. *Nat. Methods* **2020**, *17*, 261−272.
(54) Xie, Y.; Vandermause, J.; Sun, L.; Cepellotti, A.; Kozinsky, B. Bayesian Force Fields from Active Learning for Simulation of Inter-Dimensional Transformation of Stanene. *npj Comput. Mater.* **2021**, *7*, 40.
(55) Thompson, A. P.; Aktulga, H. M.; Berger, R.; Bolintineanu, D. S.; Brown, W. M.; Crozier, P. S.; in 't Veld, P. J.; Kohlmeyer, A.; Moore, S. G.; Nguyen, T. D.; Shan, R.; Stevens, M. J.; Tranchida, J.; Trott, C.; Plimpton, S. J. LAMMPS - a Flexible Simulation Tool for Particle-Based Materials Modeling at the Atomic, Meso, and Continuum Scales. *Comput. Phys. Commun.* **2022**, *271*, 108171.
(56) Hjorth Larsen, A.; Jørgen Mortensen, J.; Blomqvist, J.; Castelli, I. E.; Christensen, R.; Dułak, M.; Friis, J.; Groves, M. N.; Hammer, B.; Hargus, C.; Hermes, E. D.; Jennings, P. C.; Bjerre Jensen, P.; Kermode, J.; Kitchin, J. R.; Leonhard Kolsbjerg, E.; Kubal, J.; Kaasbjerg, K.; Lysgaard, S.; Bergmann Maronsson, J.; Maxson, T.; Olsen, T.; Pastewka, L.; Peterson, A.; Rostgaard, C.; Schiøtz, J.; Schütt, O.; Strange, M.; Thygesen, K. S.; Vegge, T.; Vilhelmsen, L.; Walter, M.; Zeng, Z.; Jacobsen, K. W. The Atomic Simulation Environment—a Python Library for Working with Atoms. *J. Phys. Condens. Matter* **2017**, *29*, 273002.
(57) Stukowski, A. Visualization and Analysis of Atomistic Simulation Data with OVITO−the Open Visualization Tool. *Modell. Simul. Mater. Sci. Eng.* **2009**, *18*, 015012.
(58) Stamatakis, M. Kinetic Modelling of Heterogeneous Catalytic Systems. *J. Phys. Condens. Matter* **2014**, *27*, 013001.
(59) Ibach, H.; Giesen, M.; Flores, T.; Wuttig, M.; Treglia, G. Vacancy Generation at Steps and the Kinetics of Surface Alloy Formation. *Surf. Sci.* **1996**, *364*, 453−466.
(60) Flores, T.; Junghans, S.; Wuttig, M. Atomic Mechanisms of the Formation of an Ordered Surface Alloy: An STM Investigation of MnCu(100). *Surf. Sci.* **1997**, *371*, 14−29.
(61) Bikaljevic, D.; Mühlegger, E.; Bonczyk, T.; Pomarolli, B.; Thaler, M.; Memmel, N. Growth and Oxidation of Zinc on Cu(111). *J. Phys. Chem. C* **2019**, *123*, 20351−20361.
(62) Kittel, C.*Introduction to Solid State Physics*; John Wiley & Sons, Inc, 2005; p 50.
(63) Briner, B. G.; Doering, M.; Rust, H.-P.; Bradshaw, A. M. Microscopic Molecular Diffusion Enhanced by Adsorbate Interactions. *Science* **1997**, *278*, 257−260.
(64) Kürpick, U.; Rahman, T. S. Tip Induced Motion of Adatoms on Metal Surfaces. *Phys. Rev. Lett.* **1999**, *83*, 2765−2768.
(65) Kurnosikov, O.; Kohlhepp, J. T.; Jonge, W. J. M. d. Can Surface Embedded Atoms Be Moved with an STM Tip? *Europhys. Lett.* **2003**, *64*, 77−83.
(66) Kolesnikov, S. V.; Klavsyuk, A. L.; Saletsky, A. M. Vacancy Formation on Stepped Cu(100) Accelerated with STM: Molecular Dynamics and Kinetic Monte Carlo Simulations. *Phys. Rev. B: Condens. Matter Mater. Phys.* **2009**, *80*, 245412.
(67) Sun, Y. S. N.; Huang, R. Z.; Gao, T. F.; Zhang, R. J.; Wang, Y. M. STM Tip-Mediated Mass Transport on Cu Surfaces. *Appl. Surf. Sci.* **2015**, *327*, 344−349.
(68) Talirz, L.; Kumbhar, S.; Passaro, E.; Yakutovich, A. V.; Granata, V.; Gargiulo, F.; Borelli, M.; Uhrin, M.; Huber, S. P.; Zoupanos, S.; Adorf, C. S.; Andersen, C. W.; Schütt, O.; Pignedoli, C. A.; Passerone, D.; VandeVondele, J.; Schulthess, T. C.; Smit, B.; Pizzi, G.; Marzari, N. Materials Cloud, a Platform for Open Computational Science. *Sci. Data* **2020**, *7*, 299.

https://doi.org/10.1021/acsphyschemau.2c00017
ACS Phys. Chem Au 2022, 2, 430−447